GRAZING-INCIDENCE TELESCOPES FOR X-RAY ASTRONOMY

R. GIACCONI, W. P. REIDY, G. S. VAIANA,
L. P. VAN SPEYBROECK and T. F. ZEHNPFENNIG
American Science and Engineering, Cambridge, Mass., U.S.A.

(Received 5 September, 1968)

Abstract. We review the progress made at our laboratory over the past several years in developing grazing-incidence imaging X-ray optics. Mirrors, detection systems and dispersion techniques are discussed and experimental results are given. We discuss the application of two telescope systems to a number of experimental observations in X-ray astronomy.

1. Introduction

In the short 6 years since its beginning, X-ray astronomy has become a powerful new tool for the study of galactic and extragalactic phenomena. It has revealed the existence of a host of objects and conditions which were not previously suspected. Many objects have been observed for which X-ray emission is one of the most important forms of energy dissipation. X-ray observations may allow the detection of the tenuous interstellar and intergalactic gas in which most matter of the universe is contained. Yet the observations which have established this new branch of astronomy have been conducted with relatively primitive instrumentation borrowed from the arsenal of high-energy physics. It is the purpose of this article to review the progress which has been made in the development of more sophisticated techniques and to discuss their application to X-ray astronomy.

Radio astronomy did not attain its present significance until about 1950, when the radio-telescope measurements first became sufficiently accurate to enable optical identifications and thus allow astronomers to determine the relationship between radio and other forms of emission. The X-ray telescopes to be discussed in this article are the first instruments capable of providing X-ray data of comparable quality, and we believe they will be as important in the development of X-ray astronomy as large antennas have been in radio astronomy.

The interstellar medium absorbs electromagnetic radiation with photon energies between the 13.5 eV hydrogen ionization energy and a few hundred electron volts. The cross-section for photo-absorption is shown in Figure 1 as calculated by BELL and KINGSTON (1967). This cross-section is shown in units of barns per hydrogen atom based on the normal cosmic abundances of the elements which comprise the principal absorbers. The flux $N(E)$ from a source can be expressed in terms of the source intensity $S(E)$ by

$$N(E) \sim S(E) \exp\left[-n_{\mathrm{H}}\sigma(E)\right],$$

where $\sigma(E)$ is the cross-section and n_{H} is the hydrogen column density in atoms per

Space Science Reviews **9** (1969) 3–57; © *D. Reidel Publishing Company, Dordrecht-Holland*

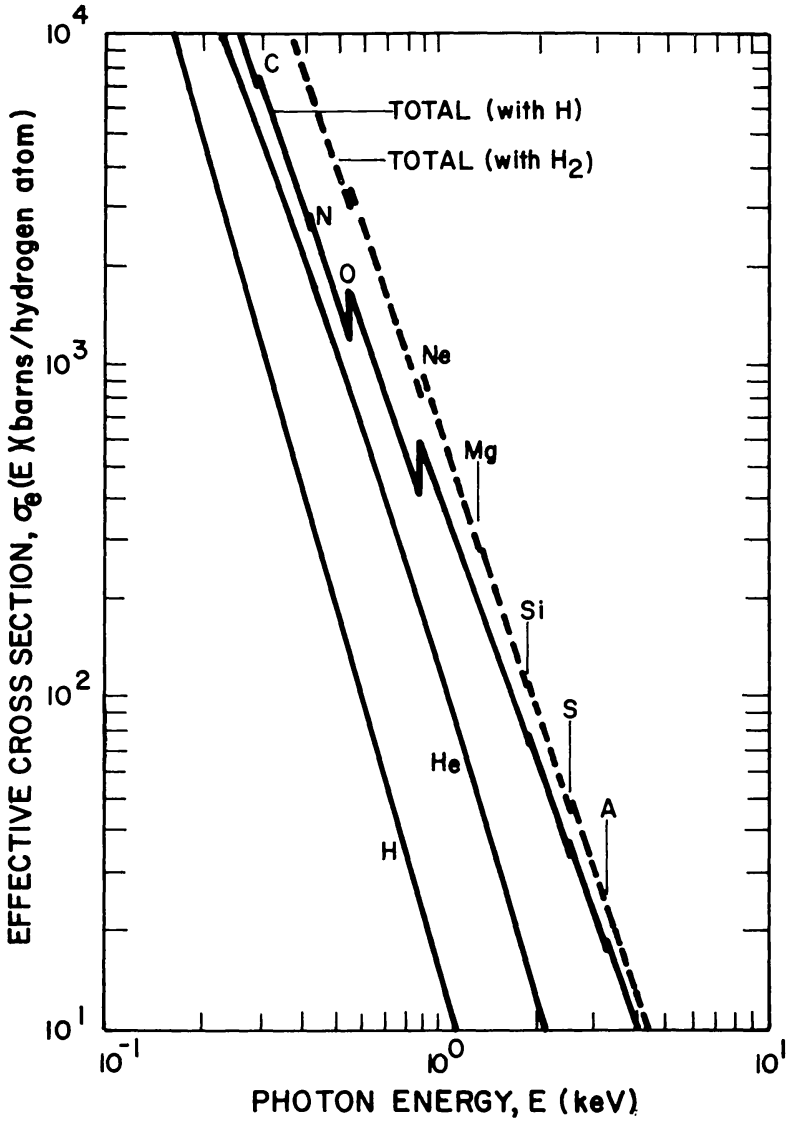

Fig. 1. Photoelectric absorption cross-section for X-rays in the interstellar medium, assuming normal cosmic abundances. (From BELL and KINGSTON, 1967.)

cm^2. The quantity $\sigma(E)$ varies approximately inversely as the 8/3 power of the photon energy between absorption edges, and it is useful to express the absorption in terms of a parameter E_0 defined by

$$\exp[-n_H\sigma(E)] = \exp[-(E_0/E)^{8/3}].$$

The absorption is thus very large for energies less than E_0 and rapidly becomes negligible for energies above E_0. The net effect is to introduce a low-energy cutoff at an energy E_0 given by $n_H\sigma(E_0)=1$.

In the vicinity of the sun, the column density of hydrogen between a source at a distance d and ourselves is approximately $(2\times10^{20}\ d/100\ \text{pc})\ \text{cm}^{-2}$; therefore, $\sigma(E_0)$ is about 5000 barns for an object at 100 pc. This distance includes a reasonable number of observable objects and results in a low-energy cutoff $E_0=280$ eV for

nearby galactic sources. At high galactic latitudes, for objects outside the galactic disk, the column density of hydrogen varies approximately as $2 \times 10^{20} \operatorname{cosec} b$, where b is the object galactic latitude. Thus, an extragalactic object above 20° galactic latitude will be observed through a column density of less than 6×10^{20} cm^{-2}, which corresponds to an E_0 of less than 450 eV. In the galactic disk, the distribution of gas is much more complex, but the column density of objects near the galactic center is between 10^{22} and 10^{23} cm^{-2}, which results in cutoff energies between 1.55 and 3.75 keV. These absorption data define the long wavelength limit of the X-ray observations; the short wavelength limit is given by the rapid decrease of flux at high energies.

Conditions resulting in X-ray emission are found in many stars. The spectral form will depend on the physical processes occurring in the emitting region. The mechanisms which may give rise to the observed celestial X-rays have been reviewed extensively (HAYAKAWA *et al.*, 1966; FRIEDMAN, 1967; GOULD, 1967; MORRISON, 1967). The source may be a hot, optically thin gas containing high-energy electrons. These electrons will excite the moderately heavy atoms of the gas, causing characteristic line radiation, and will also generate X-rays by the thermal bremsstrahlung process resulting in a continuum. The characteristic electron energy required for this process is of the order of a few kilovolts. If the electrons have a Maxwellian energy distribution, the photon number spectrum will be of the form

$$\mathrm{d}N(E)/\mathrm{d}E = 1/E \exp(-E/kt)$$

with superimposed edges and lines. Non-flare solar X-rays are probably generated by this process, and many models of the stellar X-ray sources assume such a process. The characteristic X-ray line radiation provides a means of identifying this type of source.

If the emitting object is optically thick at X-ray wavelengths and very hot, it will emit X-rays as blackbody radiation. This is an efficient mechanism and implies small, possibly short-lived objects. The required surface temperatures, of the order 10^7 K, might be found in a neutron star. The radiation would exhibit the typical blackbody spectrum and be unpolarized.

The X-rays may be emitted as a result of synchrotron radiation (magnetic bremsstrahlung) when relativistic electrons are accelerated in a magnetic field. This process is responsible for the radio emission from many sources including the Crab Nebula and probably is also responsible for the X-ray emission from the Crab. Synchrotron radiation requires a source of very high-energy electrons as the maximum emission occurs at

$$E_{\max} = 5.8 \times 10^{-9} B_{\perp} \gamma^2 \text{ (eV)}$$

and, for a field of 10 μ gauss, 10^{14} eV electrons are required for production of 2 keV X-rays. The electrons are often assumed to have a power-law energy distribution which also results in a power-law photon-number distribution, although different spectra may be produced by suitable electron-energy distributions. The radiation

from a specific region of the source is highly polarized, and there may be a net polarization of the total source radiation. Emission lines are not present.

Some forty sources have been reported up to now; these include super-Novae remnants such as the Crab Nebula, star-like objects in the galaxy, highly variable objects, and possibly an external galaxy. The X-ray emission of these objects equals or exceeds all other forms of their radiation output and is significant on an absolute scale. For example, Sco X-1, the brightest X-ray source, is thought to be about 350 pc away. The observed X-ray flux above 1 keV then implies a total emission of 6×10^{36} ergs, or more than 1000 times the emission of the sun in all wavelengths. Similarly, an X-ray source has been associated with the peculiar galaxy M-87; the reported intensities indicate an X-ray emission at energies greater than 1 keV of about 2.5×10^{43} ergs sec^{-1}. This is comparable to the total luminosity of our galaxy.

Most of our present knowledge in X-ray astronomy has been obtained with collimated proportional counter experiments. The energy resolution of the proportional counter is about 9% at 6 keV and 22% at 1 keV. This allows the general shape of the spectra to be determined but does not permit resolution of the emission lines. The typical angular resolution is of order of 1°, although strong isolated sources can be located to within a few arc minutes. This is adequate for a probable identification based on the assumption that the X-ray source is a peculiar object. This, of course, is a dangerous procedure with objects as poorly understood as the X-ray sources. There are presently only two sources, Sco X-1 (SANDAGE *et al.*, 1966; GURSKY *et al.*, 1966) and the Crab Nebula (BOWYER *et al.*, 1964; ODA *et al.*, 1967), which are identified with great confidence. There is evidence that Cygnus X-2 is correctly identified (GIACCONI *et al.*, 1967a, b). It is probable that M-87 (BYRAM *et al.*, 1966; FRIEDMAN and BYRAM, 1967; BRADT *et al.*, 1967) and possibly GX3+1 (BLANCO *et al.*, 1968; BRADT *et al.*, 1968) are correctly identified. None of the approximately 30 other sources can be associated with a visible or radio object with any degree of confidence. The angular size and structure measurements which can be made with a 1° collimator are almost meaningless. Finally, even if the sensitivity is greatly increased, the poor angular resolution may result in confusion of adjacent sources and a consequent loss of information. For example, if a counter experiment were adequately sensitive to detect Sco X-1 type sources in Andromeda, it would still be unable to resolve the several hundred such sources which would be expected to be present in a field of view; therefore, statements about the general X-ray source distribution in the galaxy could be made but individual source measurements would be impossible.

Grazing-incidence X-ray telescopes have not yet been used in stellar X-ray astronomy because of the short observational times available with rockets, the low sensitivity of the early developmental telescopes, and the lack until recently of adequate rocket-pointing controls. Rocket-pointing systems for solar studies have been available for several years, and telescopes have been used successfully to study coronal X-ray emission which at earth is orders of magnitude more intense than that from celestial sources. The first successful solar X-ray images with grazing-incidence optics were obtained in March, 1965, with a resolution of about 1 arc min (GIACCONI

et al., 1965; REIDY *et al.*, 1968). Subsequent X-ray telescope experiments by the Solar Physics Branch of GSFC (UNDERWOOD and MUNEY, 1967) and by American Science and Engineering (VAIANA *et al.*, 1968) have been performed with greatly increased resolution. Figure 2 shows the evolution in X-ray telescope performance over the past few years. The photographs obtained in 1965 had a resolution of about 1 arc min (Figure 2a). The Goddard telescope which was flown in May, 1966, achieved

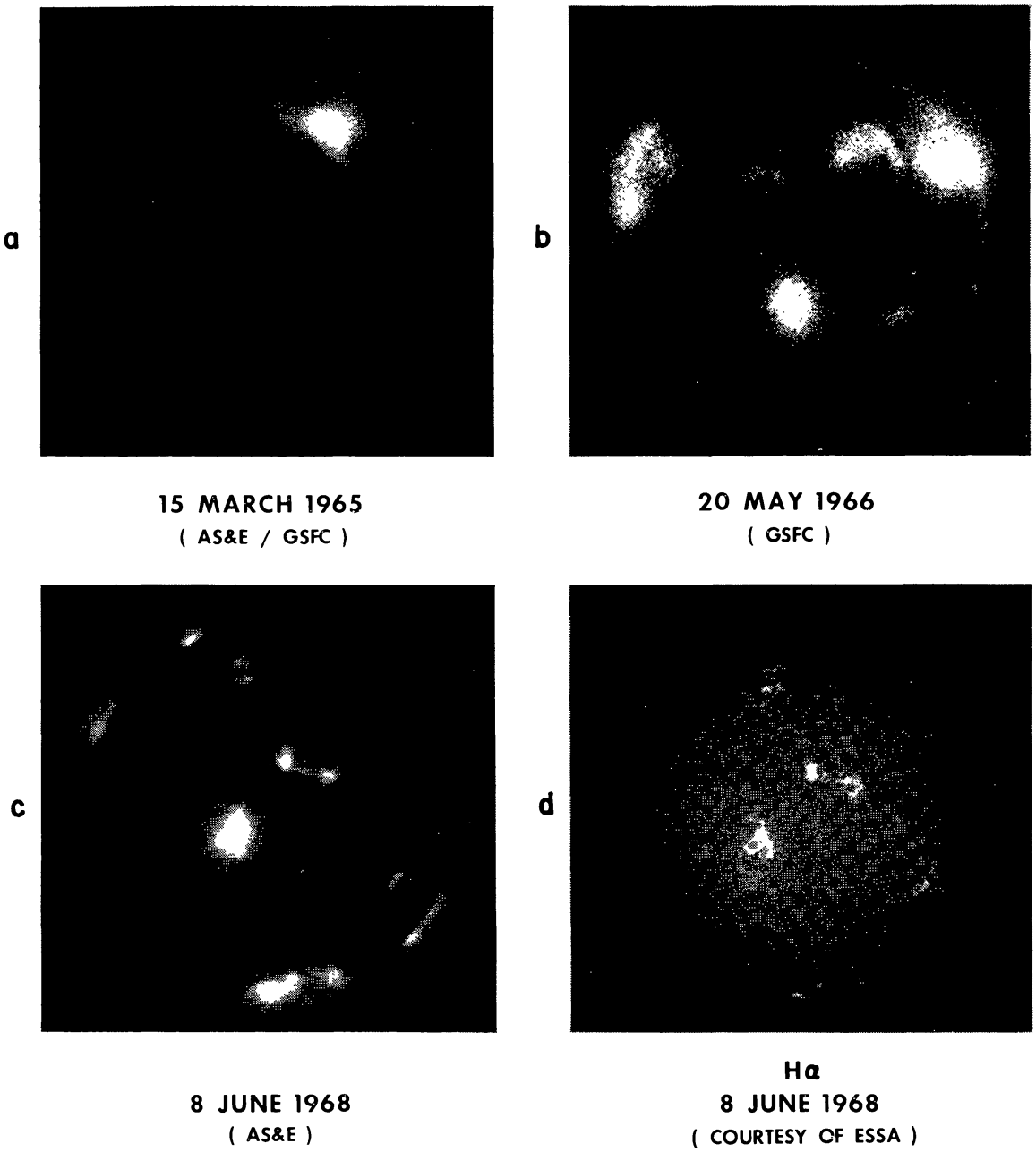

Fig. 2. Three X-ray photographs of the sun showing the evolution in X-ray telescope performance over the past few years. Also shown in an Hα picture taken at the time of the 8 June 1968 flight, illustrating the striking correspondence between the X-ray and Hα features.

a resolution on the order of 20 arc sec (Figure 2b). The latest telescope flight, which was by our group, resulted in an image resolution of a few arc seconds in the center of the field of view (Figure 2c). The importance of this increase in resolution is clearly illustrated by comparing Figures 2a and 2c. While the earlier experiment showed the enhanced X-ray emission associated with an active center and the inhomogeneity of the general coronal emission, there was no indication of the highly organized structure shown in Figure 2c. Figure 2d is an Hα photograph of the sun taken at the same time as the X-ray image in Figure 2c. The correspondence of the X-ray and Hα emission is striking. All X-ray features on the disk are identifiable in Hα. In addition, the X-ray photograph clearly shows a three-dimensional looping structure not observable in Hα. For instance, the looping structure evident in the regions near the Southwest limb shows the magnetic-field configuration linking those regions. The most interesting feature is the bright region near the center of the disk, which was an importance 1 flare. There is a detailed correspondence between the Hα and X-ray features, which indicates that the two emissions come from physically linked regions. This is surprising since the effective temperatures associated with the two emissions differ by several orders of magnitude. The two emissions may come from spatially separate regions connected by strong magnetic fields, or the flare may be a composite of small regions, presently unresolvable, as predicted by Švestka (1966). In the latter case, the emission, although originating in physically separate regions, could appear to have the same spatial distribution. We expect that the detailed analysis of these photographs will help resolve this question.

The X-ray telescope has now developed to the point where it can obtain data of fundamental importance to the study of the solar atmosphere. The potential applications to stellar astronomy are equally important. These observations include the characteristics of individual sources, the association of the X-ray sources with particular galactic structural features and galactic types, the emission of peculiar objects and the composition of the interstellar medium. A telescope observation of a source will immediately result in a position accurate to a few arc seconds, which is sufficient for an unambiguous identification with a radio or visible object or even the possible absence of any known radio or visible object at the X-ray source location. The importance of accurate locations for confidence in optical identifications is illustrated in Figures 3 and 4, which show the error boxes about the position of Sco X-1 and Cygnus X-2 respectively. (It should be noted that Cygnus X-2 is one of the X-ray sources for which we have the best location measurements.) In addition, meaningful spectral measurements will be possible so that the strongest emission lines can be detected. The sensitivity of instruments representing the next logical development in X-ray telescopes will be adequate to detect such sources in nearby galaxies, and the density of these sources in different types of galaxies can be determined. The X-ray emission of galaxies such as M-87 will be measurable, and it will be possible to determine if this emission is localized or diffused. The long-wavelength cutoff, which defines the lower energy limit of the X-ray astronomy window, will be easily measurable; and since the X-ray absorption takes place largely in the moderate

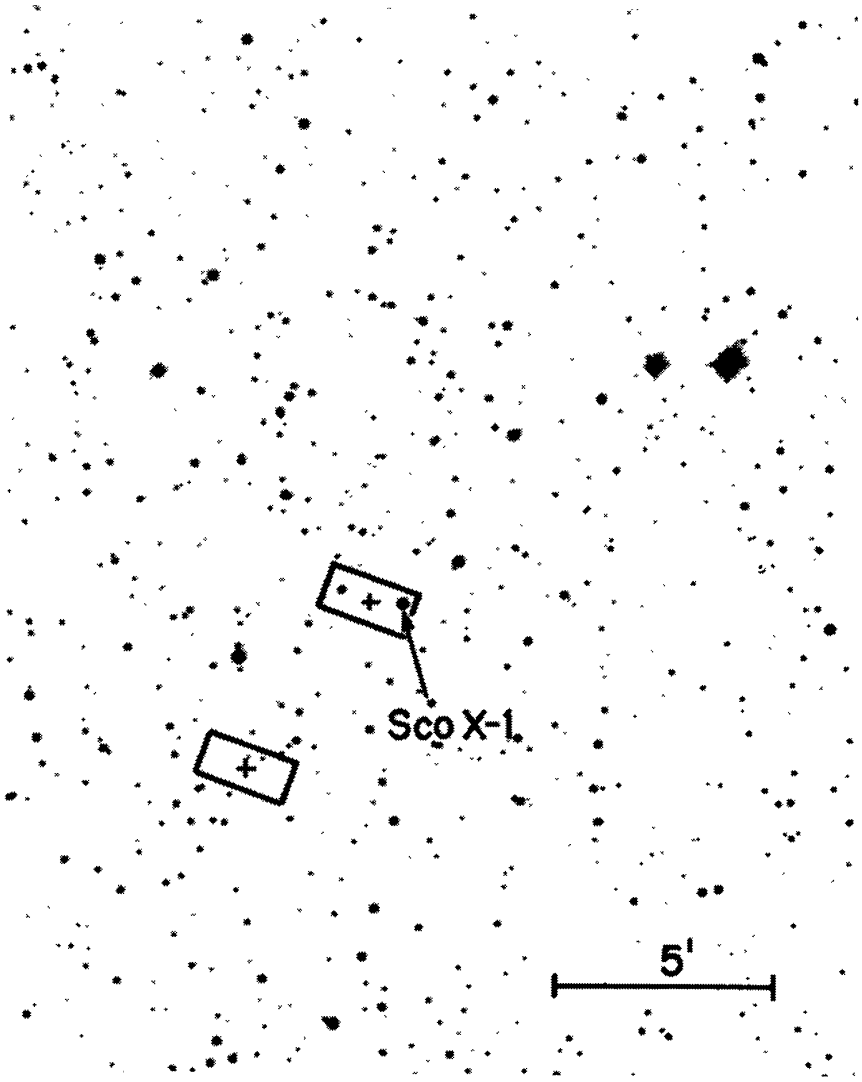

Fig. 3. Photograph of the region containing the X-ray position of Sco X-1 reproduced from a Palomar Sky survey print. The two equally probable X-ray positions as determined by GURSKY *et al.* (1966) are marked by crosses surrounded by a rectangle of 1 by 2 arc min. The object identified as the optical counterpart of the X-ray source is shown by the arrow. (SANDAGE *et al.*, 1966.)

atomic weight elements and is insensitive to the temperature of the medium over a reasonable range, it will be possible to measure the column density of these elements present in the interstellar media by detecting absorption edges.

The introduction of efficient focusing devices into stellar X-ray astronomy will extend our observational capacity so dramatically that the field may be expected to be qualitatively changed; our present list of experiments, which is based on presently studied phenomena, may not include many of the most interesting future applications. The effect of improved resolution in visible light is illustrated in Figure 5 for the spiral Galaxy M-31. The improvement obtained by the use of focusing X-ray optics can be expected to be equally dramatic.

This paper is primarily a status report on some of the devices and techniques

which we believe will be useful in X-ray telescope experiments. We have concentrated on the developments made in our laboratory because we are naturally most familiar with them. There have been contributions in this field by other laboratories, particularly the Goddard Space Flight Center Group (UNDERWOOD and MUNEY, 1967;

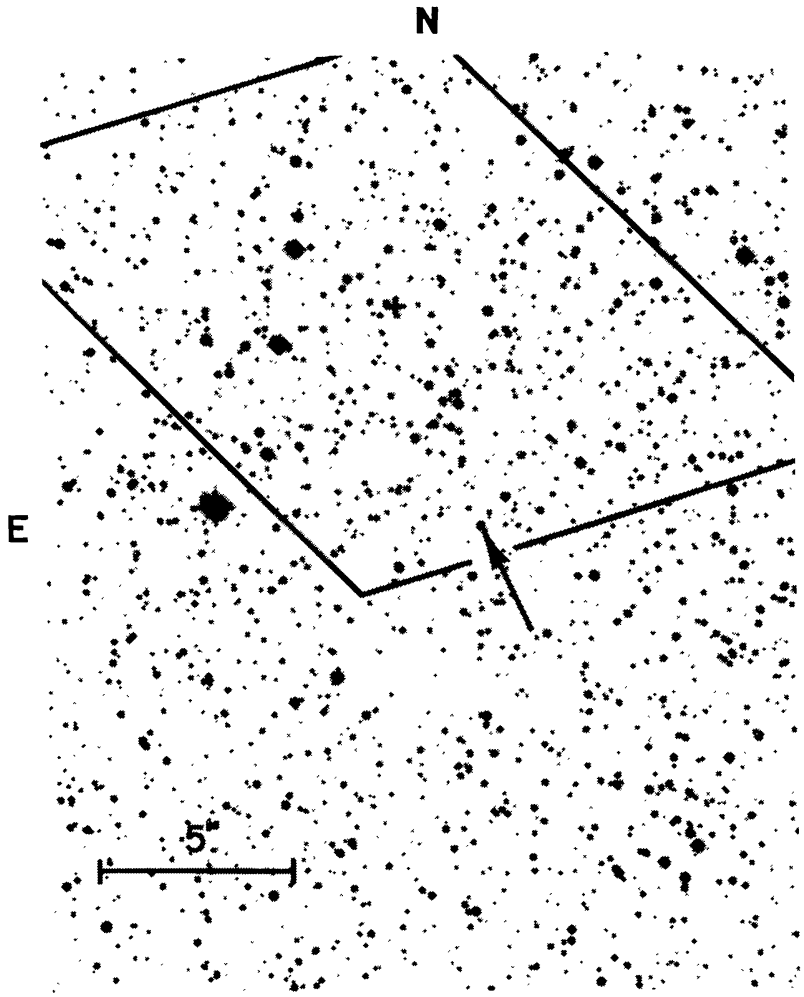

Fig. 4. The region containing the X-ray source Cyg X-2 taken from a Palomar Sky survey print. X-ray position is marked by the cross and the area of uncertainty is the trapezoid. The optical candidate is marked by an arrow. (GIACCONI *et al.*, 1967a.)

MANGUS and UNDERWOOD, 1968). The telescope mirrors are discussed in Section 2, where the design of grazing-incidence optics is considered and some optical properties of the mirrors are presented. X-ray detection techniques including film and electro-imaging devices are discussed in Section 3. Spectrographic methods and devices for use with telescopes, including transmission diffraction gratings and Bragg Crystal spectrometry, are the subjects of Section 4. Finally, in Section 5, we discuss the application of two telescope systems to a variety of experimental observations.

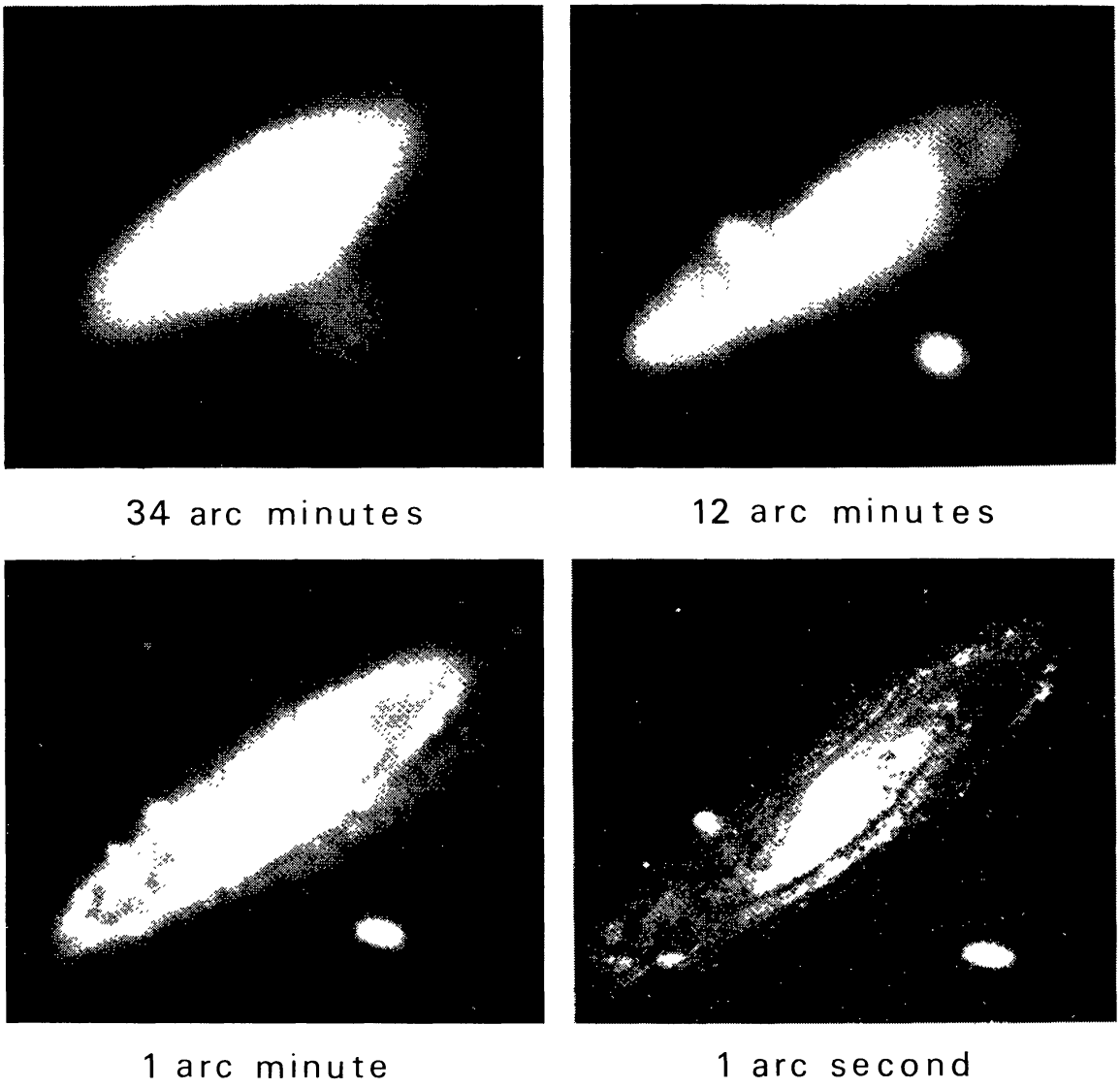

Fig. 5. A sequence of visible light photographs of the spiral galaxy M-31 taken at increasing levels of angular resolution. The improvement in X-ray photographs obtained with advanced X-ray telescopes can be expected to be equally dramatic.

2. Principles of X-Ray Imaging Systems

The design of imaging systems for use at X-ray wavelengths is limited by two severe constraints. The first is that X-rays are readily absorbed by matter; the second is that the index of refraction at X-ray wavelengths is very nearly unity. For a refractive system, these constraints imply an extremely thin lens and a very long focal length; no practical X-ray refractive imaging system has yet been devised. However, the fact that the index of refraction is slightly less than unity means that at sufficiently shallow angles of incidence total external reflection will occur. It is this principle which is the basis for the realization of the grazing incidence X-ray imaging systems. The Fresnel zone plate, which is the only other focusing device that has been used in

X-ray astronomy, was developed for use at X-ray wavelengths by MÖLLENSTEDT *et al.* (1963) and used by POUNDS and RUSSELL (1966) in a rocket flight to study solar X-rays. It is difficult to fabricate large area zone plates because of the progressively narrower zones. Also, the focal length is wavelength-dependent, which is a disadvantage in most applications.

A. THEORY OF TOTAL EXTERNAL REFLECTION

The transmission and reflection of X-rays at the boundary between two substances are described by Fresnel's equations. The index of reflection at X-ray wavelengths is conventionally written:

$$n = 1 - \delta - i\beta ,$$

where β and δ are small quantities related to the absorption and phase velocity of the radiation respectively. If β is negligible and δ positive, then radiation incident on a surface from a vacuum will be totally reflected at grazing angles of incidence less than the critical angle θ_c given by Snell's law:

$$\cos\theta_c = 1 - \delta$$

or,

$$\theta_c = \sqrt{2\delta} .$$

For radiation at a grazing angle θ and polarized so that the electric field is perpendicular to the plane of incidence, the ratio of reflected to incident power is given by an expression derived from Fresnel's equations:

$$\left.\begin{aligned} \frac{I_R}{I_0} &= \frac{(\theta - a)^2 + b^2}{(\theta + a)^2 + b^2} \\ a &= 1/\sqrt{2}\,[\sqrt{(\theta^2 - \theta_c^2)^2 + 4\beta^2} + (\theta^2 - \theta_c^2)]^{1/2} \\ b &= 1/\sqrt{2}\,[\sqrt{(\theta^2 - \theta_c^2)^2 + 4\beta^2} - (\theta^2 - \theta_c^2)]^{1/2} . \end{aligned}\right\} \tag{1}$$

The reflection efficiency for the other polarization differs negligibly from that given by Equation (1); therefore, Equation (1) also describes the reflection of unpolarized X-rays. Figure 6 shows the variation of I_R/I_0 as a function of θ/θ_c for various values of β/δ. For $\beta/\delta = 0$, the reflectivity is total for angles less than θ_c and falls off sharply at larger angles. For large values of β/δ the reflectivity is lower for $\theta < \theta_c$, but does not fall off as rapidly at larger angles.

The thickness of material which contributes to grazing-incidence reflection is small except for the case when $\theta \approx \theta_c$. PARRATT (1954) has shown that for grazing incidence at X-ray wavelengths where $\sin\theta_c \approx \theta_c$ and δ and β are small quantities, the intensity of the electric field in the reflecting medium is reduced by a factor of $1/e$ in a thickness z_0 given by

$$z_0 = \lambda/4\pi b , \tag{2}$$

where

$$b = 1/\sqrt{2}\,[([\theta^2 - \theta_c^2]^2 + 4\beta^2)^{1/2} - (\theta^2 - \theta_c^2)]^{1/2} .$$

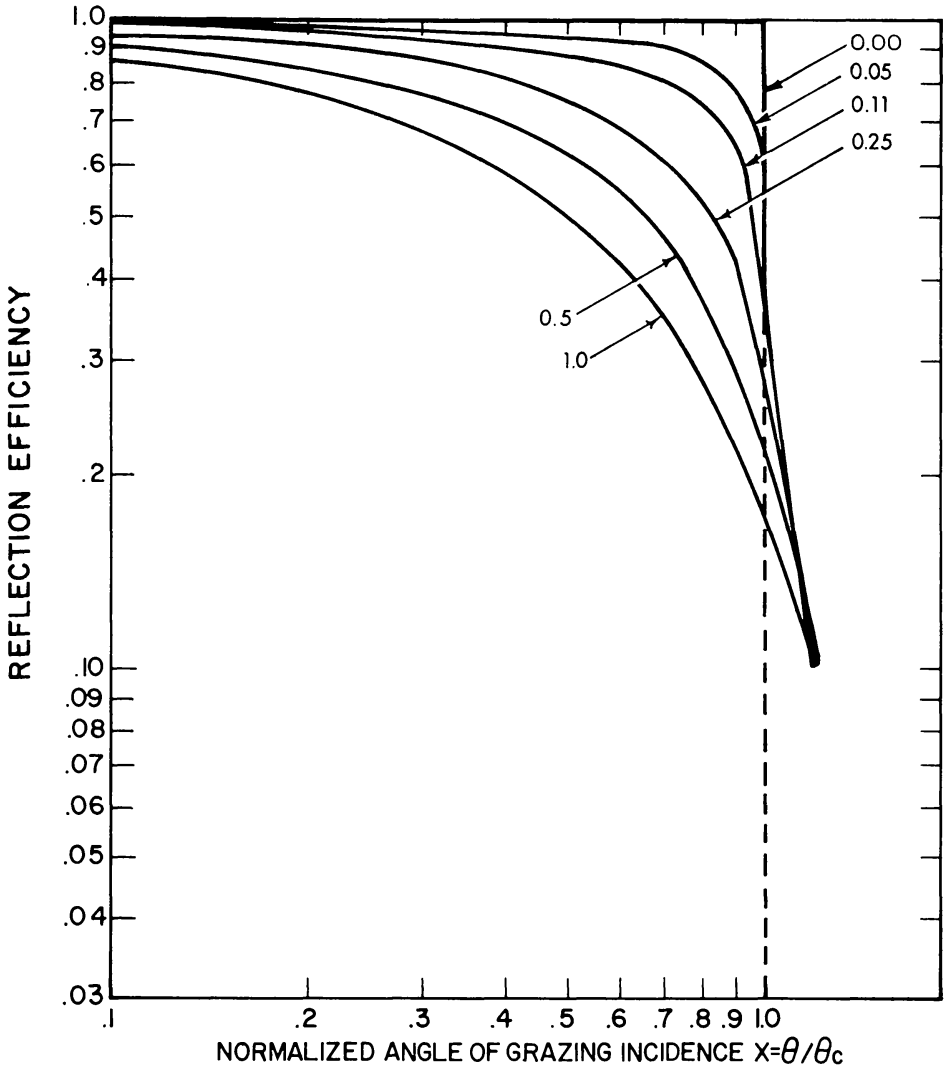

Fig. 6. Plot of reflection efficiency vs. normalized grazing angle θ/θ_c for various values of β/δ. (After HENDRICK, 1957.)

z_0 has a maximum value when $\beta=0$. In that case, for $\theta<\theta_c$:

$$(z_0)_{\max} = \frac{\lambda}{4\pi(\theta^2-\theta_c^2)^{1/2}} \approx \frac{\lambda}{4\pi\theta_c} \text{ (if } \theta \text{ is not very close to } \theta_c).$$

For the nickel telescopes discussed in this paper, θ_c will be between 1° and 2° in the wavelength region from 4 to 8 Å. Therefore, $(z_0)_{\max}$ will be on the order of 20 Å.

B. CALCULATION OF β AND δ AT X-RAY WAVELENGTHS

The quantity β describes the absorption and is related to the linear absorption coefficient μe by the expression:

$$\beta = \lambda/4\pi\,\mu = \lambda\varrho/4\pi\,[\mu/\varrho], \tag{3}$$

where λ is the wavelength, ϱ is the density, and (μ/ϱ) is the mass-absorption coefficient. Thus, β can be calculated from experimentally measured data.

δ can be determined from experimental measurements of the reflectivity at grazing incidence (HENDRICK, 1957; LUKIRSKII *et al.*, 1964; STEWARDSON and UNDERWOOD, 1965), or it can be calculated from dispersion theory (PARRATT and HEMPSTEAD, 1954; HENKE, 1960). The reflection efficiency can be calculated with sufficient accuracy using the following simplified expression for δ (COMPTON and ALLISON, 1963)

$$\delta = \frac{2\pi r_0 c^2}{\omega^2}\left[N + \sum_H N_H \frac{\omega_H^2}{\omega^2} \ln\left|\frac{\omega^2 - \omega_H^2}{\omega_H^2}\right|\right], \tag{4}$$

where r_0 is the classical electron radius, c is the velocity of light, ω is the frequency of the radiation, N is the electron density, N_H is the electron density associated with ω_H, and ω_H is the frequency associated with the absorption edge H.

For frequencies far from an absorption edge, Equation (4) reduces to

$$\delta = (2\pi r_0 c^2)/\omega^2 \, N_A ,$$

where N_A is the density of electrons associated with resonance frequencies less than ω.

Using this method, we have calculated the reflection efficiency for beryllium, aluminum, nickel and gold surfaces. The results are shown in Figure 7.

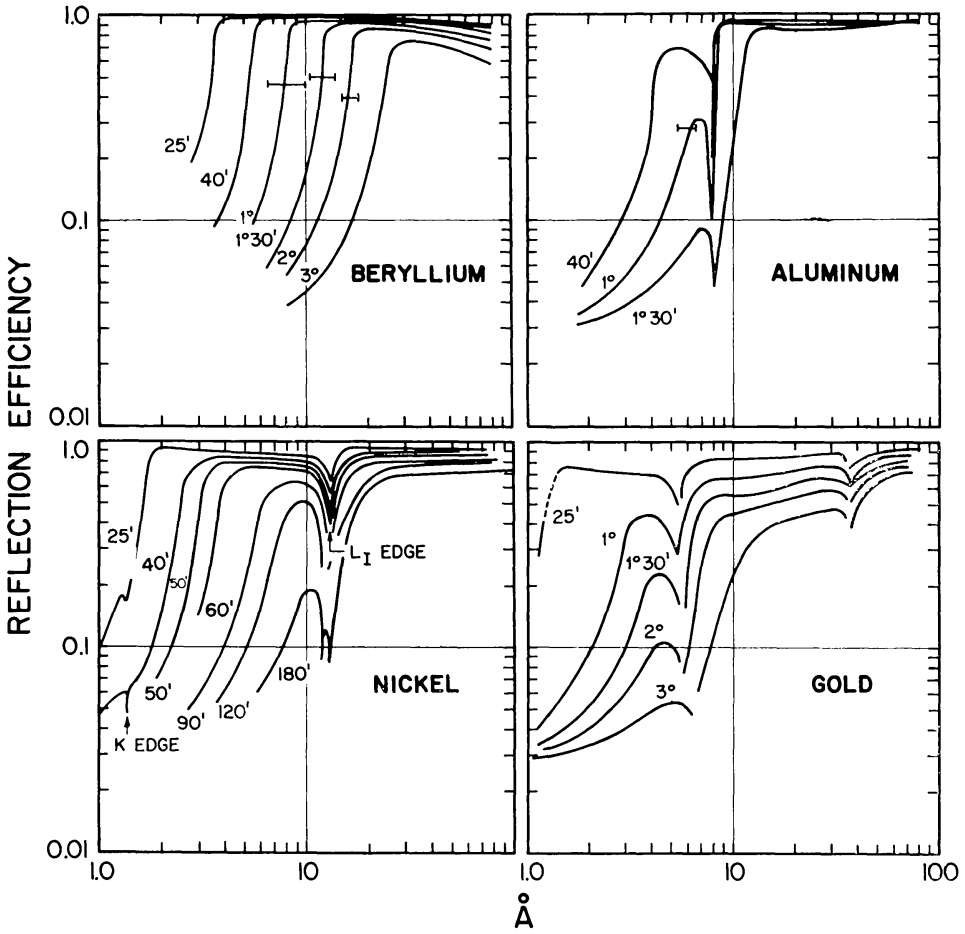

Fig. 7. Theoretical reflection efficiency vs. wavelength for various grazing angles and reflection materials.

In general, experimental measurements of the X-ray reflectivity at grazing angles of incidence have been in good agreement with theory. Discrepancies may be attributed to surface properties such as oxidation, porosity, or annealing (PARRATT, 1954), which become increasingly important with increasing wavelength. One exception is the paper by YONEDA (1963), which reports the observation of two reflected beams: one at a reflection angle equal to the angle of incidence; the second at a smaller grazing angle. However, several papers (NIGAM, 1965; GUENTERT, 1965; WARREN and CLARKE, 1965) appear to have established that Yoneda's result is due to the nature of surface and/or the angular divergence of the X-ray beam.

C. IMAGING SYSTEMS

The use of paraboloidal mirrors at grazing incidence in X-ray astronomy was first proposed by GIACCONI and ROSSI (1960). The paraboloid has the geometric property that paraxial rays will be imaged to a point at the focus of the paraboloid. However, the condition of grazing incidence implies that the far zone of the paraboloid must be used as a reflecting element. It is not possible to satisfy the Abbé sine condition for such a system (or for any other single reflection system at grazing incidence) and, thus, the image will be subject to severe comatic aberration. WOLTER (1952a, b) has shown that this aberration can be removed by the addition of a second reflecting surface, an hyperboloid, which is confocal and coaxial with the paraboloid. The focal plane is then moved to the nearer of the two foci of the hyperboloid. Wolter has also shown that the Abbé sine condition can be satisfied more exactly by increasing the number of reflecting surfaces in multiples of two. A grazing-incidence imaging system cannot be constructed with an odd number of reflecting surfaces. KIRKPATRICK and BAEZ (1948) have shown that real images can also be formed by successive reflection from two perpendicular mirrors. MCGEE (1957) has successfully demonstrated the use of this system in X-ray microscopy. Wolter considered three general systems of conic sections, which are shown in Figure 8.

The X-ray telescopes which we have developed are all of the internally reflecting paraboloid-hyperboloid configuration (Figure 8a). This design minimizes the difficulty of maintaining alignment between the two elements and maximizes the reflection efficiency for a system of a given focal length and diameter. Typically, the reflecting surfaces are pitched at angles of 40 to 80 arc min to rays which are incident parallel to the axis. The general equations for such a system can be written in the coordinate system of Figure 9 as:

$$\left.\begin{array}{ll} \text{Paraboloid} & y^2 + z^2 = 4p(x + p + c + k) \\ \text{Hyperboloid} & \dfrac{(x+k)^2}{h^2} - \dfrac{y^2 + z^2}{c^2 - h^2} = 1 \end{array}\right\} \tag{5}$$

In order to maximize the two surface reflection efficiency, we impose the condition $\alpha = \varrho$, so that a paraxial ray will strike the first and second reflecting surfaces at about the same angle. With this condition, the four constants in Equation (5) may be

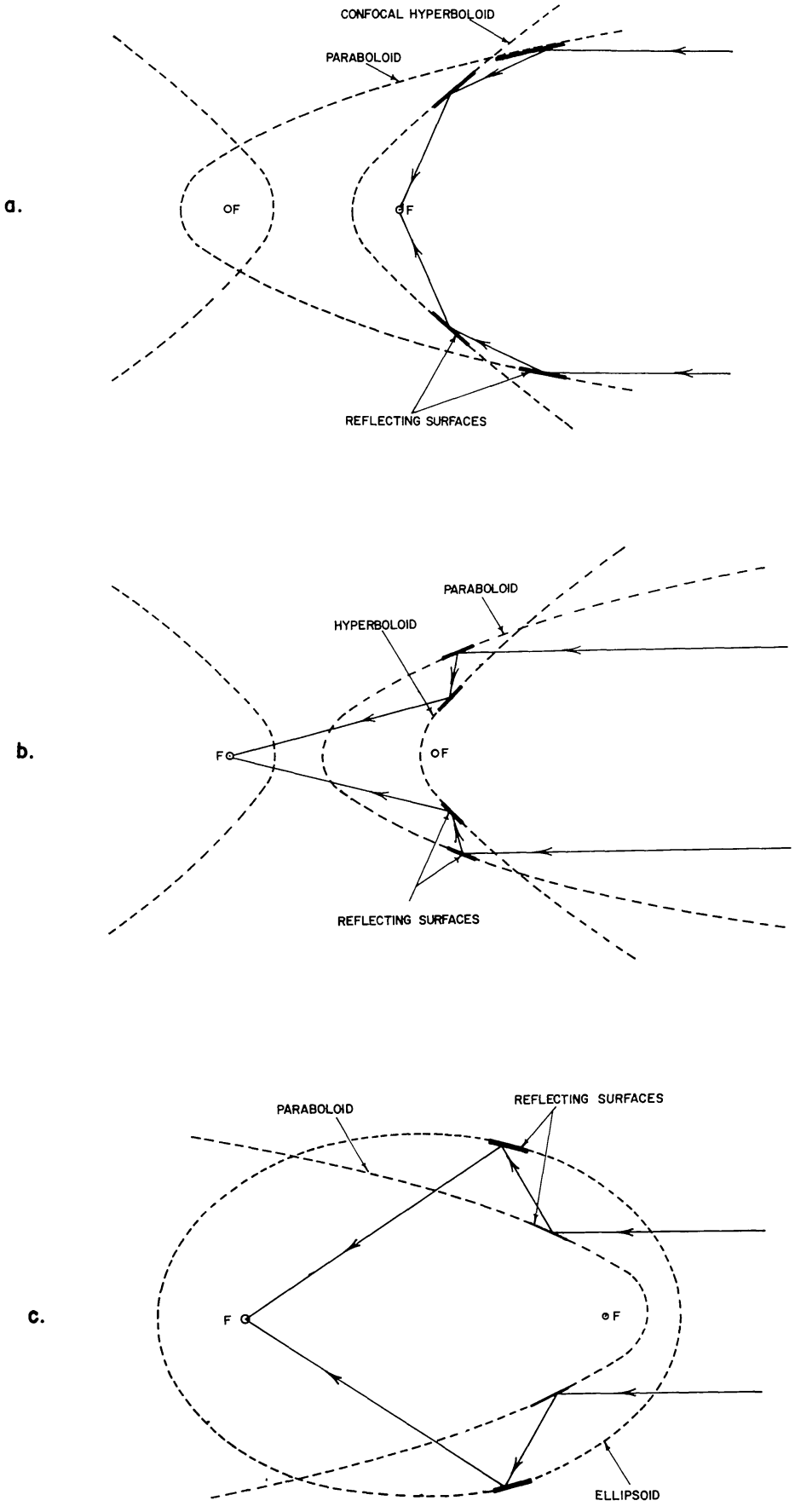

Fig. 8. Three possible configurations for image-forming X-ray telescopes suggested by WOLTER (1952a, b).

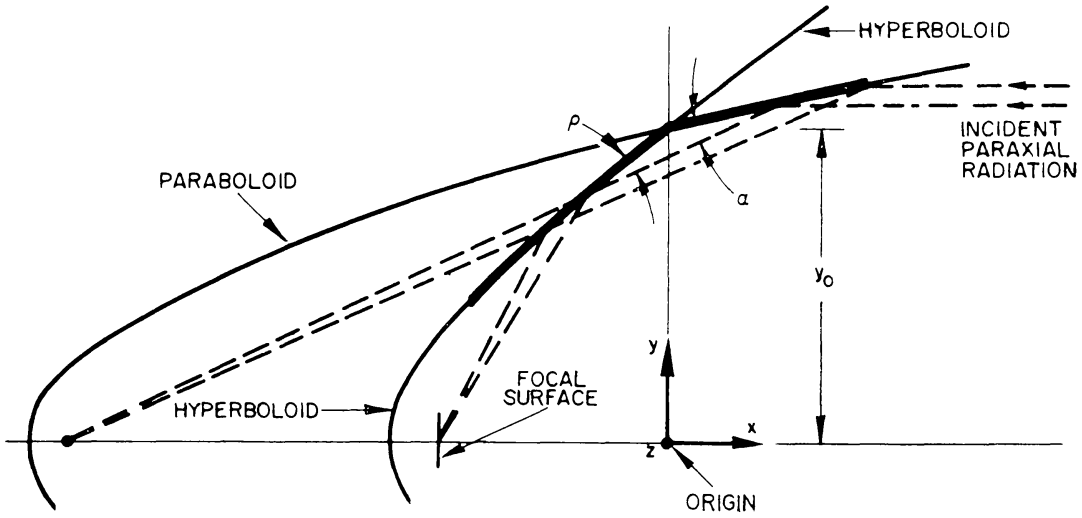

Fig. 9. Schematic cross-section of the type of telescope commonly used in AS&E experiments.

expressed in terms of two initial design parameters: the focal length F, which is the distance from the intersection plane $x=0$ of the paraboloid and hyperboloid to the nearer focus of the hyperboloid; and the radius y_0 of the telescope surface in the plane $x=0$. These expressions are:

$$p = y_0^2/8F$$

$$c = F/2$$

$$k = 3/2F$$

$$2h^2 = c^2 + k^2 + 4p(p + c + k) - \left[(c^2 + k^2 + 4p(p + c + k))^2 - 4c^2k^2\right]^{1/2}.$$

If L is the length of the paraboloidal reflecting surface along the optical axis, the geometric collecting area A is:

$$A \approx \pi y_0^2 L/2F.$$

A suitably positioned pair of aperture stops is used to prevent the undesired rays which do not strike the reflecting surfaces or strike only one of the surfaces from reaching the image area. In one arrangement which we have used, disk-shaped stops are placed in the plane $x=+L$ and $x=-L$. In another, the stops are placed in the principal plane $x=0$ and at a pseudo-focus formed by the hyperboloid at approximately $x=-\frac{2}{3}F$.

The imaging properties of this type of mirror system have been evaluated with a ray-tracing program. Figure 10 shows three blur circle plots for a typical telescope design ($F=20y_0$; $L=2y_0$) corresponding to parallel bundles of rays incident 0, 5, and 10 min off-axis. Each parallel bundle consists of 60 rays incident on the paraboloid in such a way that each ray represents an approximately equal amount of the area of the paraboloid. The on-axis plot is a geometrical point. Off-axis, the high density of points at the center of each plot indicates that the intensity distribution within the blur circle is sharply peaked at the center. Thus, the imaging properties of a given

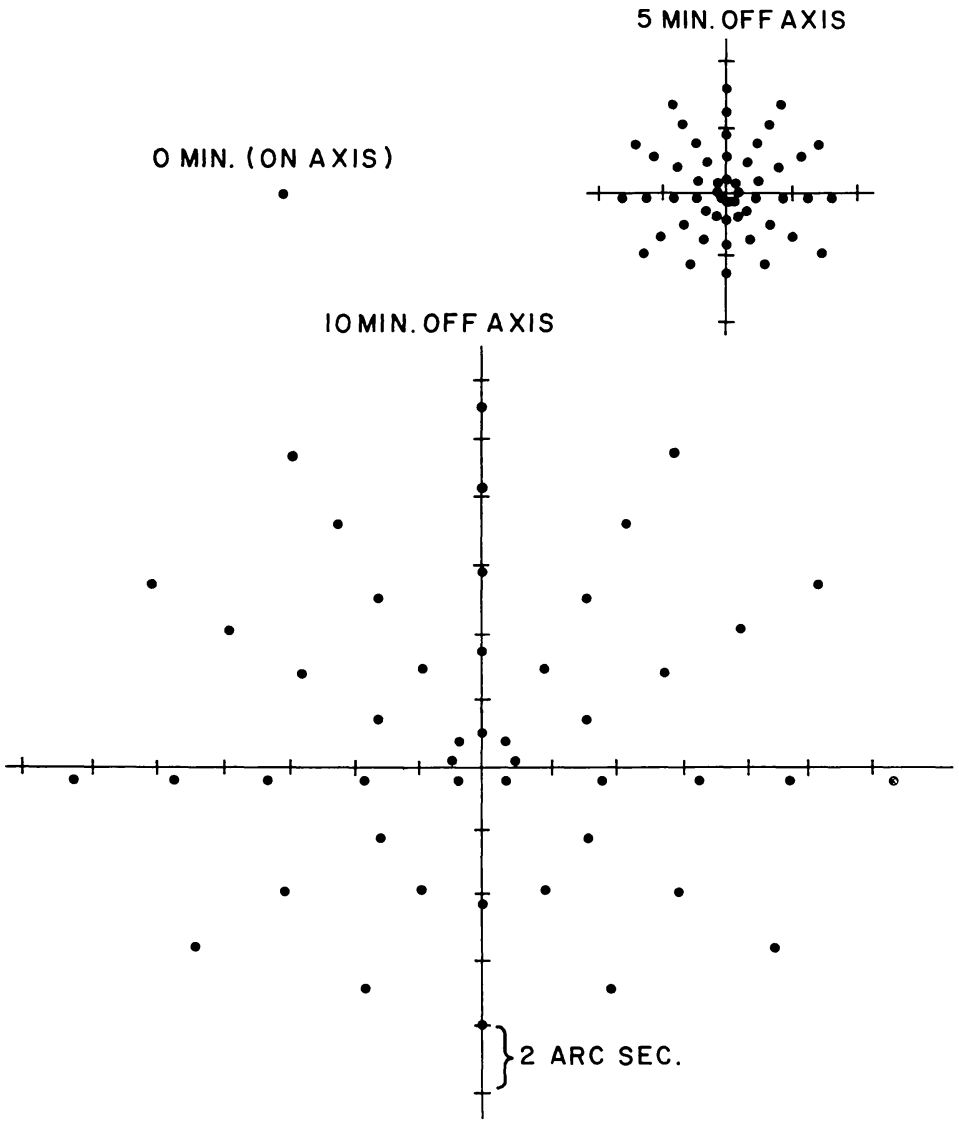

Fig. 10. Blur circle plots for rays incident 0, 5, and 10 min from the axis for a telescope with $F = 20y_0$, $L = 2y_0$. The on-axis plot is a geometrical point. Some rays are missing from the 5 and 10-min plots because of geometrical vignetting by the mirror surfaces and the aperture plates. A flat focal surface was used.

system are considerably better than would be indicated by the diameters of the blur circles. It was also found that the rays striking near the center of the blur circle had been reflected from points near the intersection plane of the paraboloid and hyperboloid; that is, near the principal plane. For other rays, the distance from the center of the blur circle was approximately proportional to the distance of the reflection points from the principal plane. Thus, if the other dimensions are held constant, the diameter of the blur circle at a given distance off-axis is directly proportional to the length of the reflecting surfaces L. Blur circle diameter vs. distance from the axis for a flat focal surface passing through the focus of the hyperboloid is plotted in curve A of Figure 11.

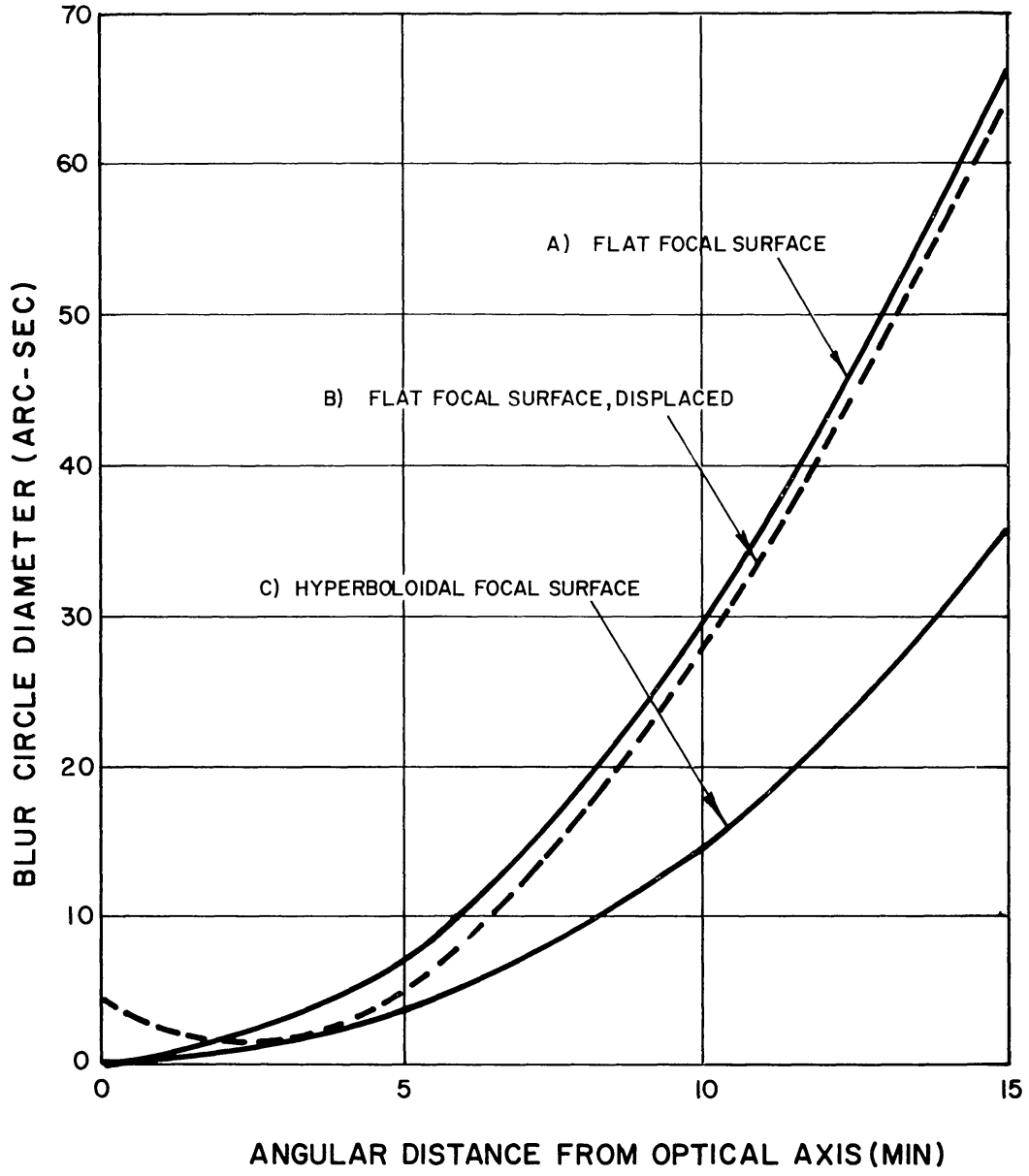

Fig. 11. Total blur circle diameter vs. angular distance from the optical axis, from a ray tracing done on a telescope system with the characteristics $F = 20y_0$ and $L = 2y_0$.

By comparing the striking points of the rays in the blur circle with the corresponding points of reflection from the mirror surfaces, it was found that the diameter of any of the blur circles, except, of course, the on-axis one, could be decreased by translating the focal plane slightly forward. Curve *B* of Figure 11 shows the result of a shift of $1.8 \times 10^{-4} F$, an amount sufficient to minimize the diameter of the 3-min off-axis blur circle. Since the magnitude of the optimum shift was found to vary with the distance from the axis, the best focal surface is obviously a curved one. The required curved surface could be approximated closely with an hyperboloid. Curve *C* corresponds to the optimum hyperboloidal focal surface. The improvement at a given distance off-axis is a factor of 2 compared to the original flat surface.

The full diameter of the field of view is limited both by geometrical vignetting due to the aperture stops and shape of the reflecting surfaces and by the requirement on the grazing angle of reflection. The field of view of a telescope whose surfaces are pitched 43 arc min to its axis is shown in Figure 12, which is an X-ray exposure. The real image extends over a diameter of about 50 arc min; but, of course, the angular resolution at the edges of this field is poor because of geometrical aberrations.

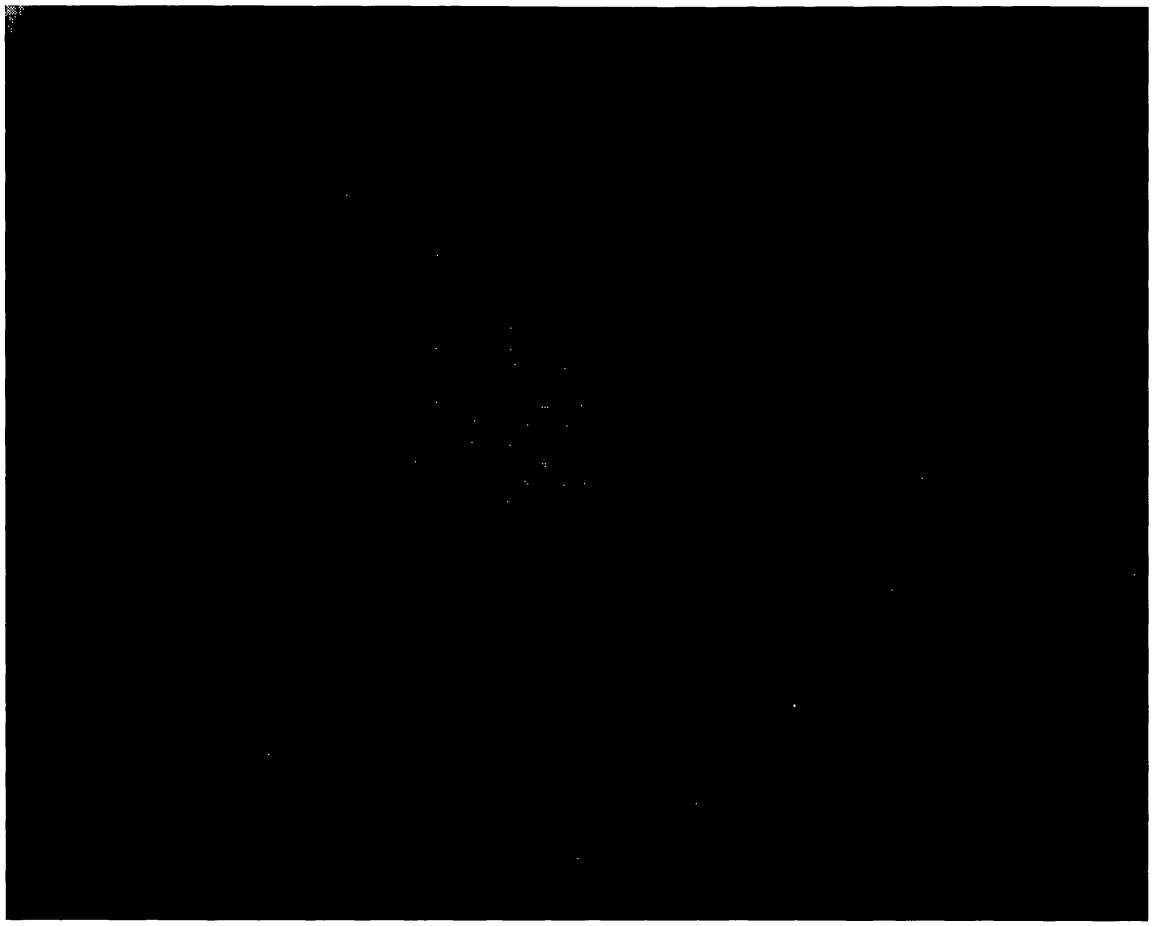

Fig. 12. An X-ray exposure illustrating the full extent of the usable field of view. The real image is the square array of dots in the central area. The pattern of arcs at the edge is not part of the real image and is due to rays that were reflected from the hyperboloid but not the paraboloid. Since the dots are spaced 3 arc min center-to-center, the full diameter of the field of view is about 50 min. (The square array of dots was formed by placing a device which we call the Multibeam Collimator between the telescope and a broad X-ray source. This is a type of mechanical collimator which transmits in a large number of equally spaced directions rather than in only one.)

D. DIFFRACTION EFFECTS

The diffraction pattern from a thin annular aperture is a series of concentric rings. The angular distance θ_m to the first minimum is given by $\theta_m = 0.38\lambda/y_0$, where λ is the wavelength and y_0 the radius of the annulus. For the telescopes discussed in this paper θ_m is on the order of 0.3 arc sec at $\lambda = 5000$ Å and 6×10^{-4} arc sec at $\lambda = 10$ Å.

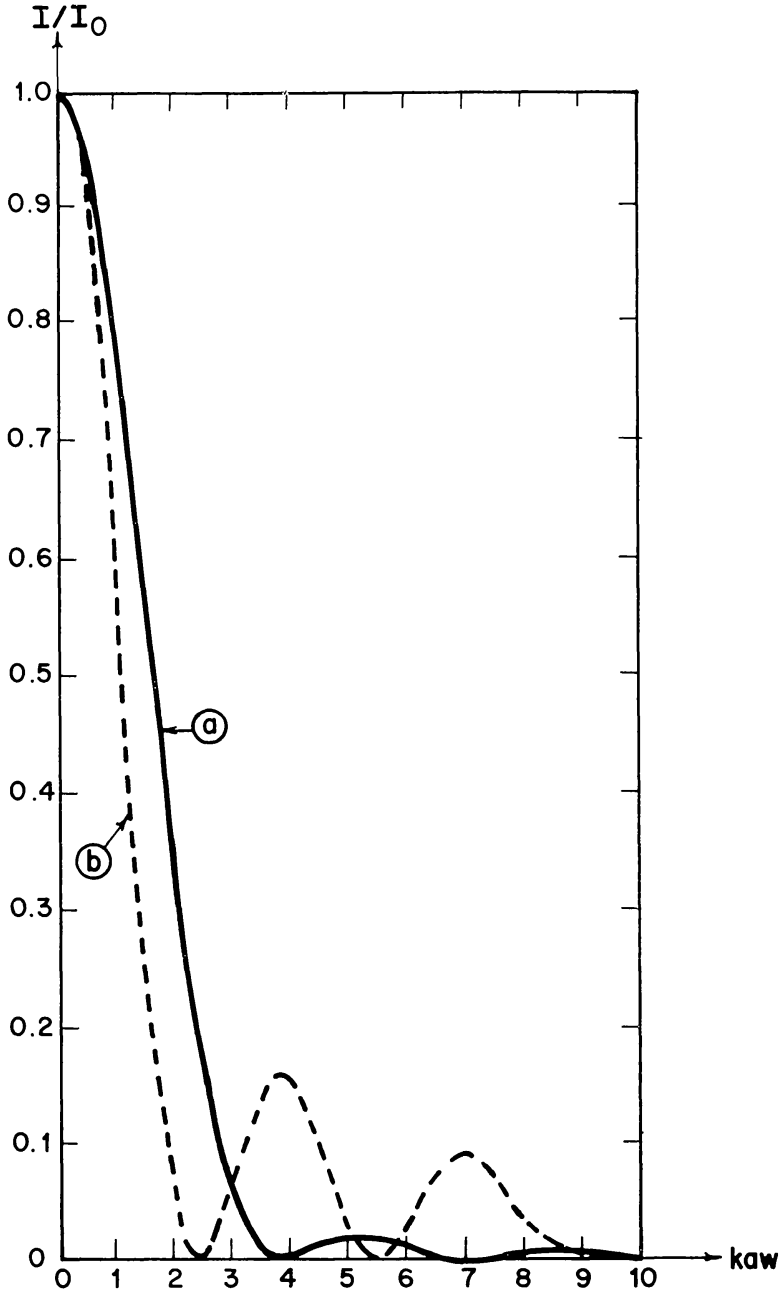

Fig. 13. Diffraction pattern from a circular aperture (a) and from an infinitely thin annular aperture (b). Here $k = 2\pi/\lambda$, a is the radius of the aperture, and w is the sine of the angular distance from the center of the diffraction pattern. Although the annular aperture of an X-ray telescope is not infinitely thin, the diffraction pattern through the first few maxima would differ only negligibly from (b). (After STEWARD, 1928.)

The diffraction pattern from a thin annular ring is shown in Figure 13, which also shows for comparison the diffraction pattern of a circular aperture.

E. EARLY TELESCOPES

A representative sample of the types of earlier X-ray telescopes we have built and flown is shown in Figures 14 and 15. The first telescopes, such as those shown in

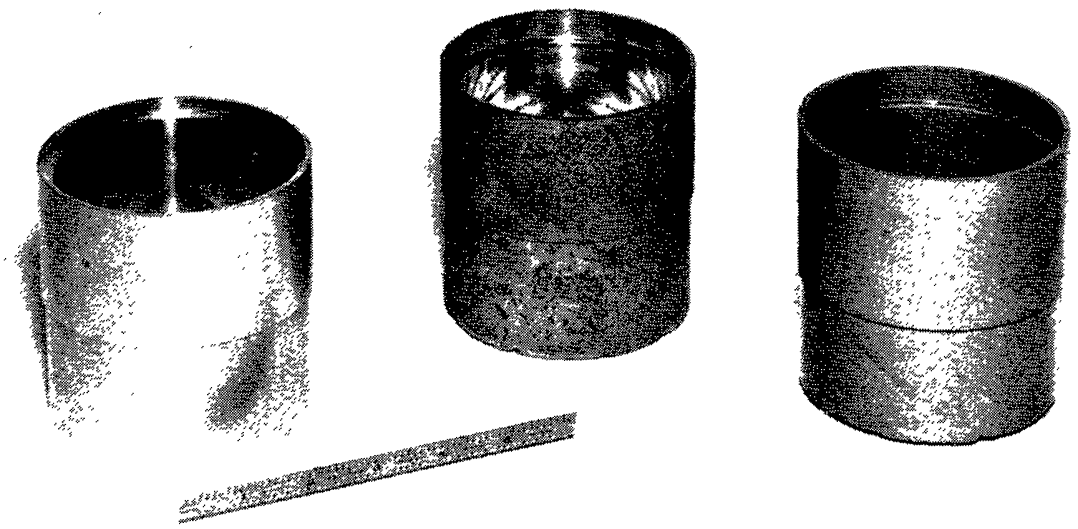

Fig. 14. Three early telescopes produced by epoxy casting and conventional machining methods. The angular resolution was several arc minutes and the efficiency less than 1 %.

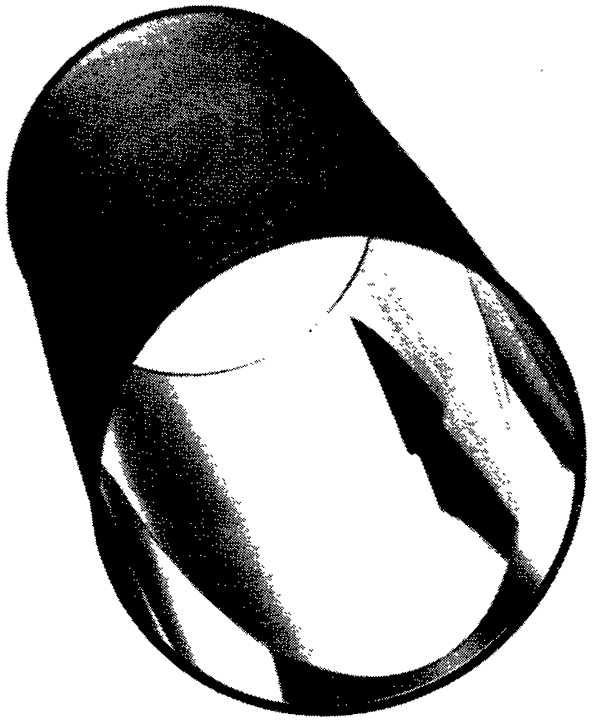

Fig. 15. Nickel telescope which was electroformed on an optically polished stainless steel mandrel and then removed. The collecting area is 2 cm^2; the diameter is 7.5 cm; and the focal length is 84 cm. The reflection efficiency at 8.3 Å is about 20 % when all of the energy within several arc minutes of the image is included.

Figure 14, were made of aluminum using ordinary machining techniques or of epoxy which was cast in machined molds. The angular resolution was limited to several arc minutes and the efficiency was less than 1% because of poor control over both the gross and local surface shapes. Three of these units, flown on a sounding rocket in 1963, produced X-ray pictures of the sun, which contained indistinct images of the principal plage region that was present (LINDSAY, 1965).

Telescopes of the next generation, such as the one in Figure 15, were made of nickel which was electroformed on optically polished stainless steel mandrels. Several telescopes were made from each mandrel and required no additional machining or polishing after removal from the mandrel. However, because the nickel telescope walls were of necessity thin, roundness was not normally maintained to better than 25 microns after removal from the mandrel. The reflection efficiencies of these telescopes were measured by a technique which included all of the rays striking within several arc minutes of the center of the image. The efficiency at 8.3 Å was about 20% compared to a theoretical value of 69% for double reflection from nickel surfaces pitched at a grazing angle of 40 min. The angular resolution was 20–30 arc sec, although finer details could sometimes be resolved at low contrast. Telescopes of this type have been flown on OSO-4 (PAOLINI *et al.*, 1968) and on a sounding rocket flight on 17 March, 1965 (REIDY *et al.*, 1968). One of the photographs from the rocket flight has been shown in Figure 2a.

F. PRESENT STATE-OF-THE-ART

Examples of the most recent type are shown in Figure 16. Figure 16a shows a telescope which was flown on 8 June 1968 and produced the picture of the sun shown in Figure 2c. The system in Figure 16b will be flown on AS&E's Apollo Telescope Mount (ATM) experiment. Two nested confocal elements, each consisting of a paraboloid and an hyperboloid, are used to increase the collecting area. The reflecting surfaces of these telescopes are thin layers of Kanigen, a nickel alloy, which is deposited on a thick aluminum or beryllium support structure. These mirrors were ground, figured and polished using fairly conventional optical fabrication techniques.*

1. *Resolution and Surface Tolerances*

Since the diffraction limit in the X-ray region is very small, the angular resolution is presently limited by attainable surface tolerances and finish. We have found that the resolution is relatively insensitive to local surface finish, and thus is limited by the surface tolerances. A typical set of tolerances for recent mirrors, specifically the ATM system, is illustrated in Figure 17. The tolerances were selected to achieve an angular resolution of 3 arc sec.

The most natural arrangement for the set of tolerances on the mirror surfaces is one that is closely tied to the test and measurement techniques used. Because imaging

* Polishing and figuring of these Kanigen surfaces has been performed by Diffraction Limited, Inc., Bedford, Mass., whose personnel have contributed substantially to recent advances in X-ray telescope fabrication methods.

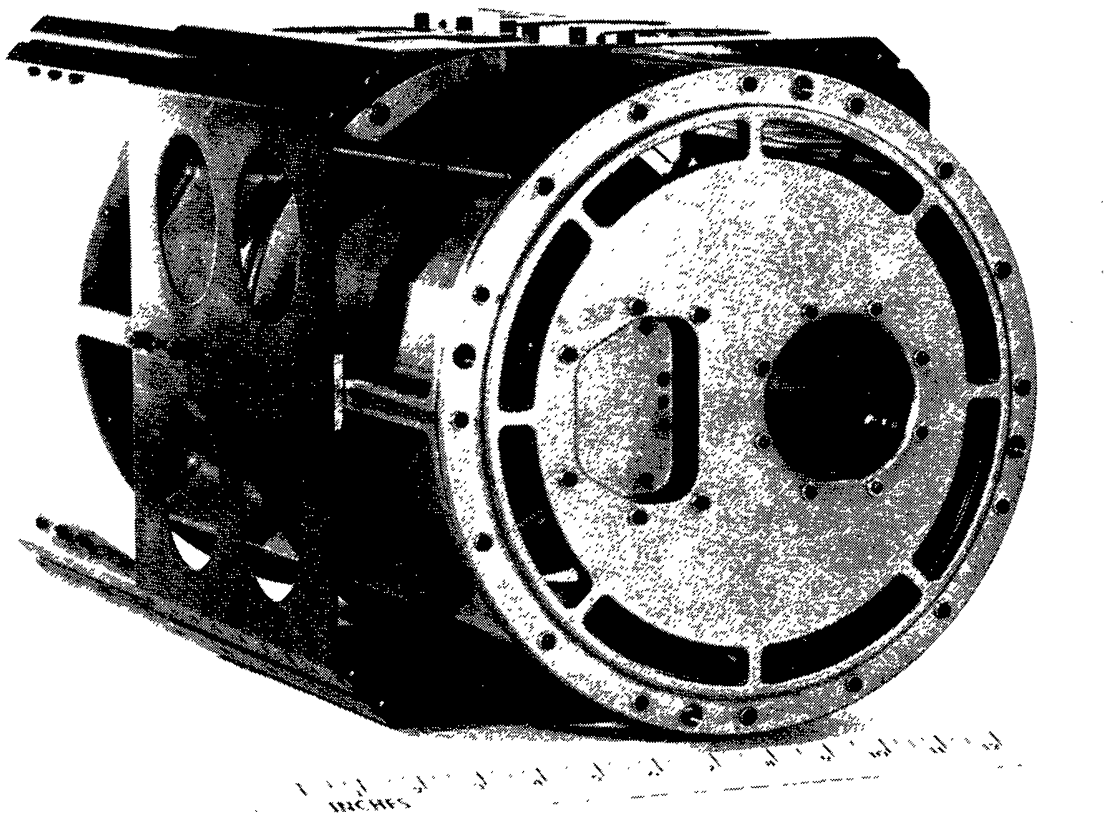

Fig. 16a. The 23-cm diameter Kanigen telescope which produced the X-ray picture of the sun shown in Figure 2c. The collecting area is 34 cm^2 and the focal length is 132 cm. The X-ray resolution is illustrated in Figure 18.

tests using visible light are not sufficiently sensitive to the surface defects in mirrors used at grazing incidence, we have relied on separate measurements of various surface dimensions using precision mechanical methods and optical test plates. The magnitude of the tolerances on the different dimensions of the reflecting surfaces can vary widely and still be consistent with a given design goal. Thus, the tolerances on R, ΔR, and $S(x)$ for the mirror section shown in Figure 17 range over more than 2 orders of magnitude, from $\pm 7.5 \times 10^{-3}$ cm to $\pm 1.3 \times 10^{-5}$ cm. The three parameters R, ΔR, and $S(x)$ control the profile of the mirror. Here R is the radius, ΔR is the difference in radii of the two ends (and thus controls the average slope), and $S(x)$ is the departure of the surface from a cone as a function of x. The dimensions R and ΔR are measured using precision mechanical techniques; $S(x)$ is determined by placing a glass test plate of known profile in contact with the reflecting surface and observing the pattern of interference fringes. The seemingly loose tolerances on R and ΔR are actually consistent with the stringent $S(x)$ tolerance. Consider, for example, the result of changing the radius R of the inner ATM paraboloidal mirror by the full 7.5×10^{-3} cm allowed within the tolerance. The resulting surface is no longer a para-

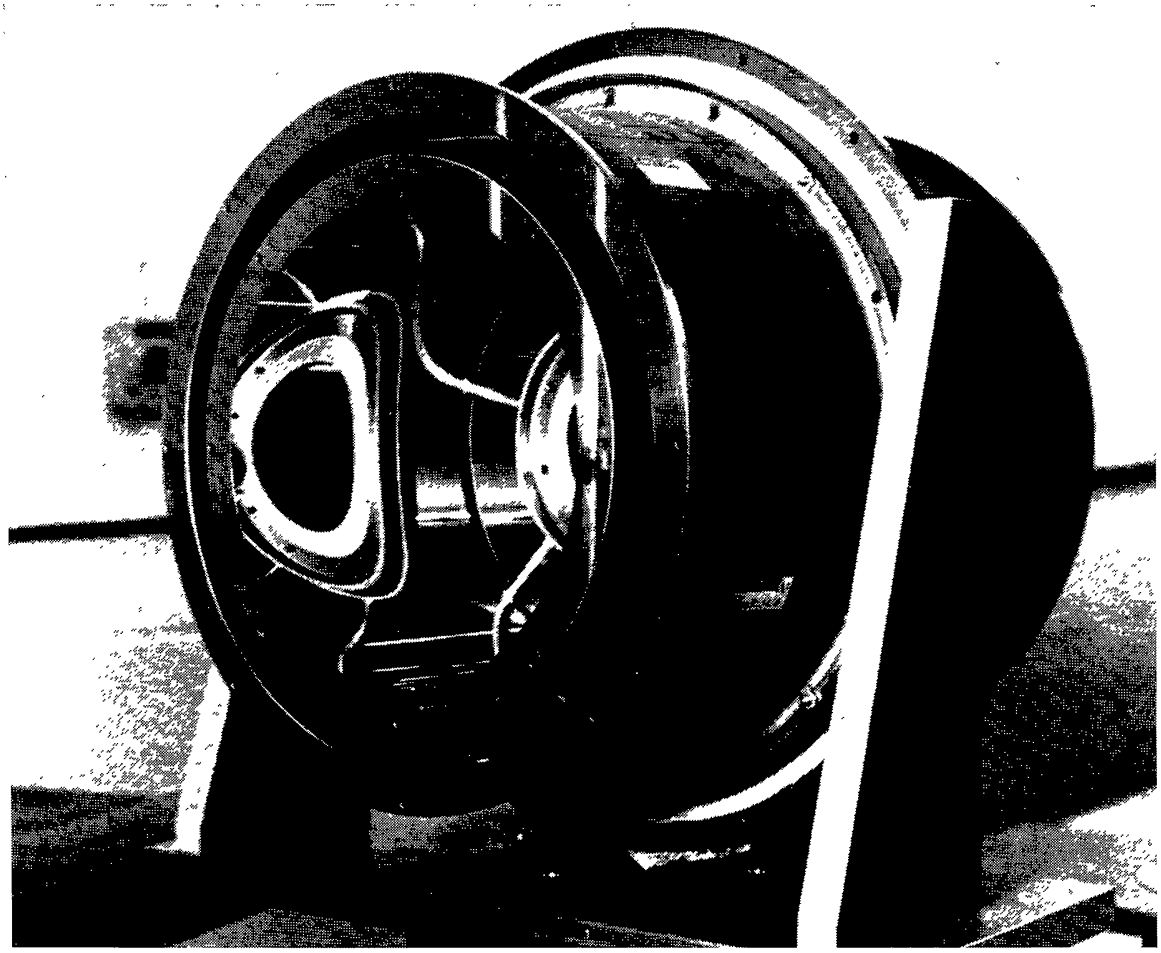

Fig. 16b. Recently completed telescope system for ATM. The combined collecting area of the nested confocal 23 and 31 cm diameter mirrors is 44 cm^2. The focal length is 213 cm. The distorted reflection of the small telescope, which will form an image on the face of the image dissector, can also be seen.

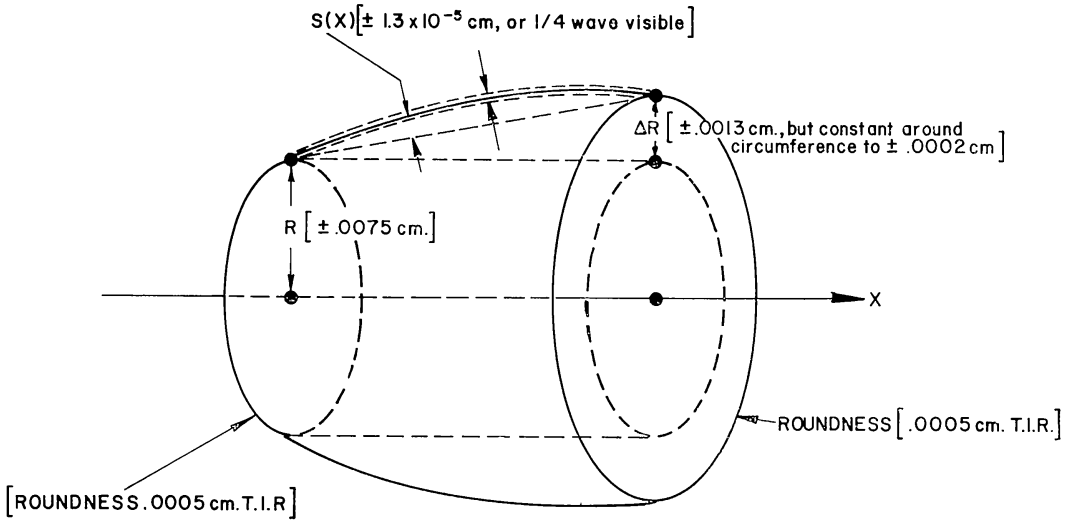

Fig. 17. The surface tolerance on each dimension of the ATM mirror surfaces is shown in the brackets adjacent to the dimension. These tolerances are consistent with a resolution of a few arc seconds.

boloid; but a new paraboloid can be fitted to it to within 4×10^{-7} cm, which is much closer than the tolerance on $S(x)$. The only noticeable effect would be a slight change in the focal length. Varying ΔR within the limits of its tolerance would have a similar effect.

There are also two tolerances on the symmetry of the surfaces: roundness, and the variation of ΔR around the circumference. These tolerances are inter-related in that the roundness tolerance on the two ends of the surface automatically sets an upper limit on the possible variation of ΔR around the circumference. However, the variation of ΔR around the circumference is more critical than roundness. This is because the former controls the slope of the reflecting surfaces, while the latter controls only the position. A change in the radial position of the reflecting surface by an amount δR, without changing the slope, will move the striking points of the rays in the focal surface by δR; but changing ΔR by the same amount will move the striking points by a factor of $2F/L$ times as much. The factor $2F/L$ is typically on the order of 10. So, instead of putting a needlessly stringent tolerance on roundness which would be adequate to control the variation of ΔR as well, the two tolerances are usually specified separately.

The limiting tolerance on the resolution of the ATM mirrors is a symmetry tolerance: the variation of ΔR around the circumference. The tolerances on R, ΔR, $S(x)$ and roundness are each adequate to contain the reflected rays within a 5 arc sec blur circle after two reflections. At the time that the ATM mirror was designed the tightest tolerance which could realistically be placed on the variation of ΔR around the circumference allows blur circle diameters of up to 12 arc sec after two reflections. This variation is compatible with an angular resolution of 3 arc sec, since the intensity distribution is sharply peaked near the center of the blur circle. The variation of ΔR in most of the completed ATM mirror elements is smaller than the allowed tolerance by a factor of 2–4.

Figure 18 is a laboratory test at 8.3 Å of the resolution of the telescope shown in Figure 16a. This telescope, made to a slightly lower tolerance level than the ATM system, can clearly resolve point sources separated by 7 arc sec center-to-center. However, the fact that details finer than 7 arc sec were visible in pictures of the sun made with this telescope on the flight of 8 June 1968 indicates that the resolution was limited by the laboratory test arrangement rather than by the telescope. Therefore, we conclude that the present fabrication techniques are adequate to achieve a resolution of a few arc seconds.

2. *Efficiency and Surface Finish*

The traditional Rayleigh criterion for a perfect reflecting surface is satisfied if surface irregularities introduce errors in the reflected wavefront of less than $\lambda/4$. At a grazing angle of incidence θ, the height h of a surface deviation corresponding to a $\lambda/4$ wavefront error is:

$$h = \lambda/8\theta .$$

For $\lambda = 12$ Å and $\theta = 1°$, the allowable height h is 85 Å.

The irregularities on our present mirror surfaces greatly exceed the Rayleigh criterion in the X-ray region. As described in the previous section, the tolerance on $S(x)$ allows a height of up to 1300 Å for slowly varying irregularities which extend over major areas of the mirror surface, although, in fact, this height has been reduced

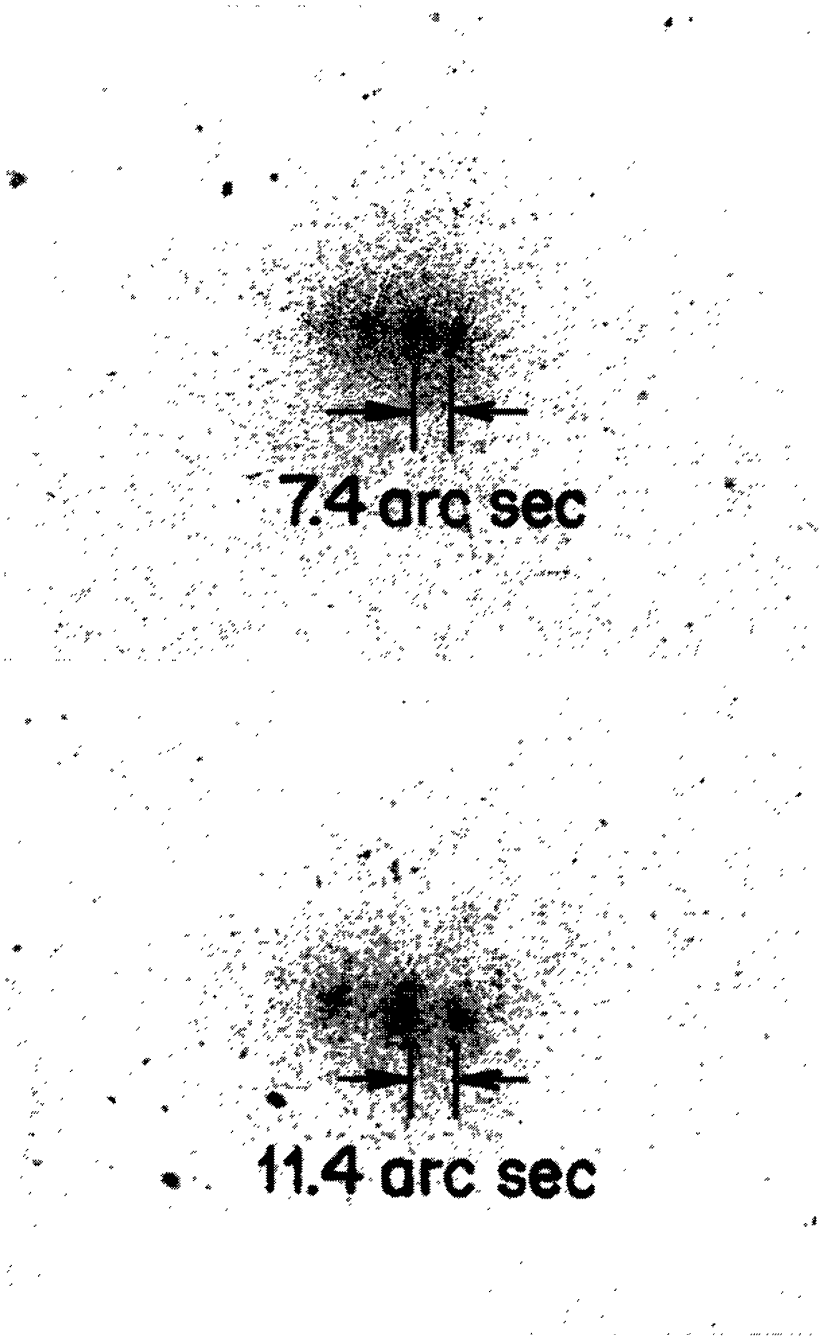

Fig. 18. Two exposures showing the resolution of the telescope of Figure 16a at 8 Å. The film (Panatomic-X) was moved back from the normal focal plane in order to focus on the sources, which were 20 m from the entrance aperture rather than at infinity. The fact that details on the order of 2 or 3 arc sec were visible in pictures of the sun made with this telescope on the flight of 8 June 1968 indicates that the resolution shown here was limited by the laboratory test arrangement rather than by the telescope.

to 500 Å over most of the surface of some of our ATM mirrors. The effect of these irregularities is to produce small angular errors in the ray paths of a few arc seconds. However, there are also irregularities on a local scale which characterize that ill-defined quality called 'surface finish'. The effect of these local irregularities is to modify the intensity distribution in the image plane on a scale of arc minutes or more, rather than arc seconds. Since the reflections are grazing ones, this redistribution occurs in highly ordered way. Figure 19 shows a group of over-exposed images of a point source made with a 44° sector of an X-ray telescope. The other 316° of the circumference were blocked by a mask. The radiation scattered or reflected out of the central areas of each image is redistributed into well-defined fan-shaped patterns, whose vertex angles are equal, within 2%, to the 44° angle of the telescope sector which was used. The effect of a rib, which was part of the mounting structure of the telescope and happened to lie in the middle of the 44° sector, can be seen as a dark lane which bisects the fan patterns. (Similar dark lanes caused by mounting ribs can be seen around the image of the solar flare in Figure 2c.) On the basis of the orientation

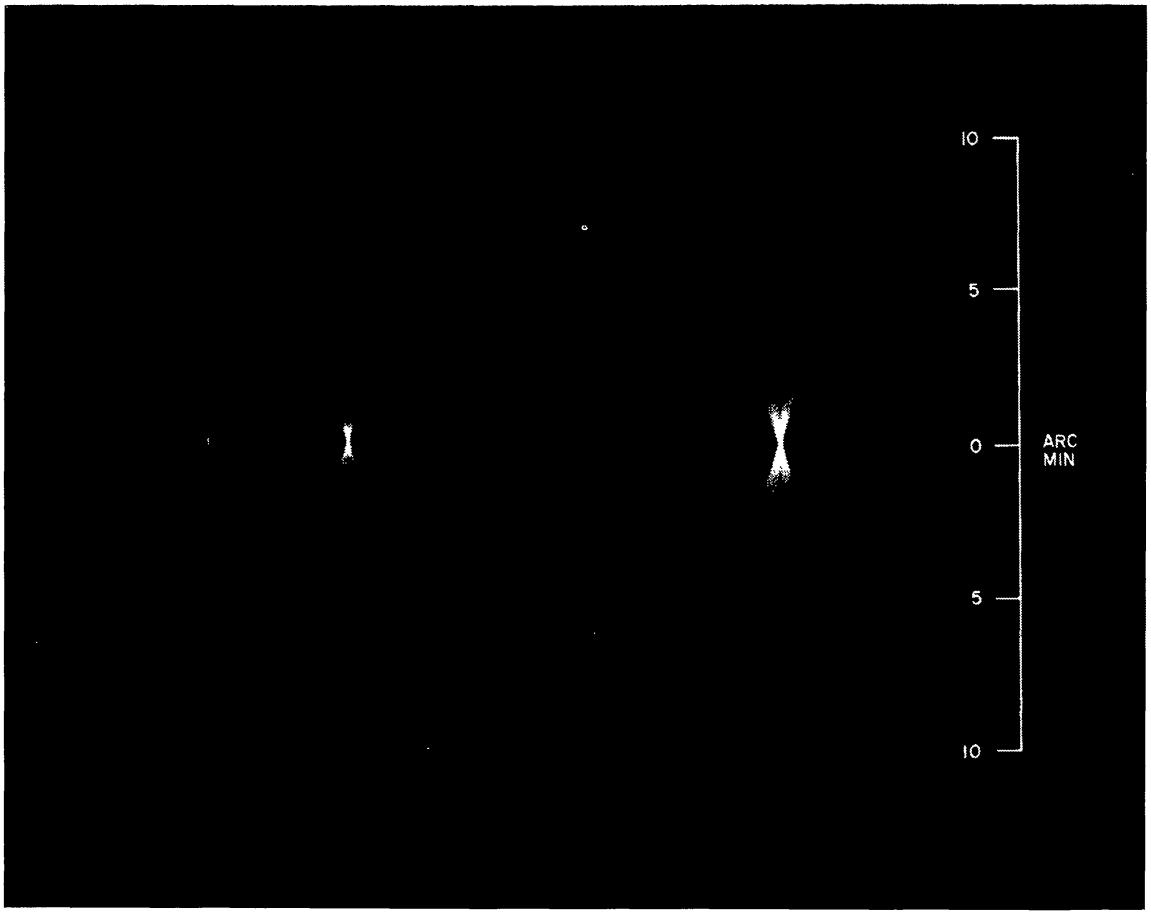

Fig. 19. Over exposed X-ray images of a distant point source made with a 44° sector of an X-ray telescope. The other 316° of the circumference was blocked by a mask. The orientation of the fan-shaped patterns indicates that rays scattered or reflected out of the proper image element by surface irregularities are confined almost entirely to the plane of incidence.

of these patterns, we conclude that the rays scattered or reflected out of the proper image element by surface irregularities are confined almost entirely to the plane of incidence of the incoming ray.

It can be shown that this effect is a consequence of the fact that the reflections are grazing ones, whether the deviations are considered to be diffraction from surface irregularities or ordinary specular reflection. The former interpretation has been discussed by ELLIOTT (1963) and EHRENBERG (1949). Let the irregular surface profiles in directions parallel to and perpendicular to the plane of incidence be described by sums of a distribution of spatial frequencies. Because of the foreshortening effect of grazing incidence, any of the spatial frequencies Ω associated with the surface profile parallel to the plane of incidence will appear to the incident radiation to be increased by a factor of $1/\theta$. The resulting angular deviation η of the ray from its correct path due to diffraction from this grating-like surface will be:

$$\eta \approx (1/\theta)\lambda\Omega = \lambda/\theta\Lambda \approx 60\lambda/\Lambda \qquad \text{for } \theta \approx 1^\circ, \tag{6}$$

where $\Lambda = 1/\Omega$. However, the spatial frequencies associated with the surface profile perpendicular to the plane of incidence will appear unchanged to the incident rays. Then, the deviation perpendicular to the plane of incidence will be λ/Λ, or 60 times smaller than the deviation in the plane of incidence. Even if the deviations are considered to be the result of specular reflection from surface irregularities, this result still holds. A ray specularly reflected from a surface element tilted at a small angle σ from the perfect surface will be deviated from the correct path by an angle 2σ if the deviation is in the plane of incidence. Leaving the amount of tilt unchanged, if the orientation of the tilted element is now changed so as to deviate the ray as far as possible out of the plane of incidence, the angular deviation becomes $2\sigma\theta$, or 60 times smaller than before, assuming a θ of 1°.

We have made measurements at 8.3 Å of the small angle scattering from the surfaces of the Kanigen telescope shown in Figure 16a. The measurements were made out to 10 arc min from the image center and thus include much of the area of the fan-shaped patterns of Figure 19. Twenty percent of the energy in the image plane falls within 15 arc sec of the image center. However, the total energy within 10 arc min of the image center is between 10 and 20% of the incident energy. Since the theoretical double reflection efficiency at the grazing angles involved is 50%, the difference must be due to scattering at angles larger than 10 arc min or to additional absorption due to the difference between the theoretical and the actual surface.

From Equation (6), ray deviations in the plane of incidence in the observed 1–10-min range would involve surface irregularities on the scale of 2×10^{-2} cm and 2×10^{-3} cm respectively. An independent upper limit on the height of these irregularities of 1300 Å (provided by measurements of the interference fringe pattern between the Kanigen surface and a polished glass test plate) implies a length-to-height ratio of greater than 150. On the other hand, if the deviations are considered to be the result of specular reflection, slope errors of $\frac{1}{2}$ min and 5 min would be required. Combining this with the requirement imposed by the Rayleigh criterion, that the

height must be greater than 50–100 Å in order to have any effect on the imaging properties, a characteristic length for the irregularities of greater than 7×10^{-4} cm is indicated. In either case then, the irregularities needed to account for the radiation within 1–10 min of the center of the image are long and shallow ones. At present we have not been able to develop a more direct technique for observing irregularities of this type on X-ray telescope surfaces.

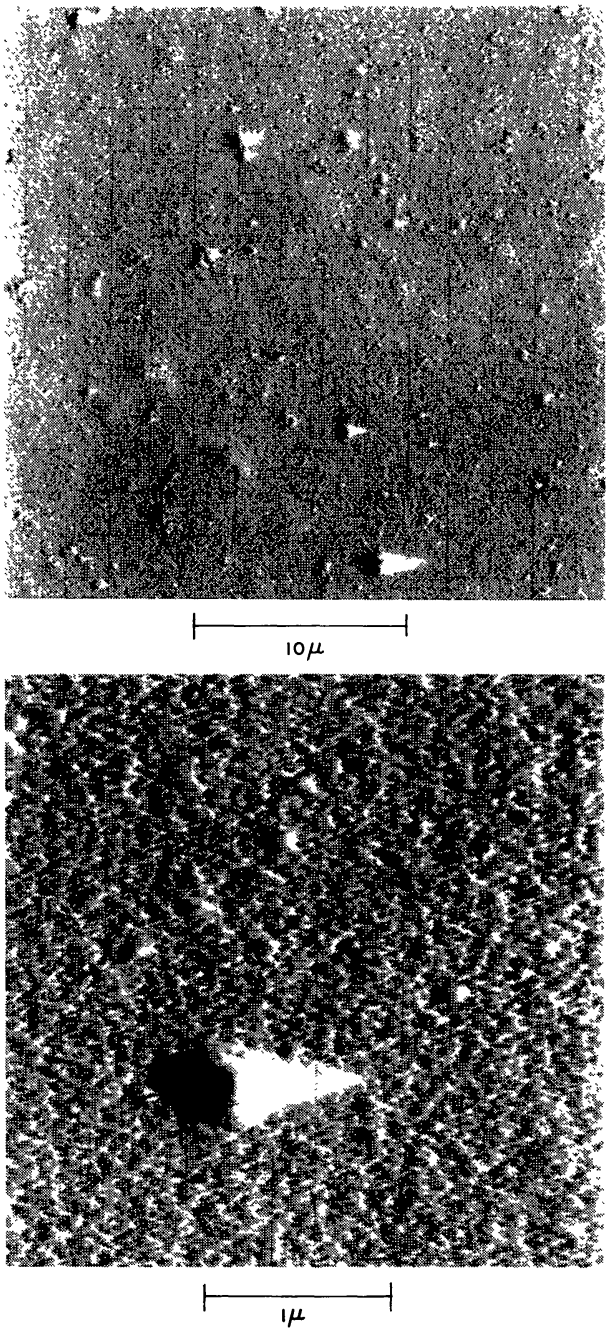

Fig. 20. Electron microscope pictures of a region of a Kanigen telescope surface shown in two magnifications. Surface roughness with a length of 100–200 Å is evident.

Surface imperfections on a much smaller scale can be observed with electron microscopy. The best X-ray imaging surfaces we have obtained to date have small-scale surface irregularities with a height of 100–200 Å. Figure 20, an electron micrograph of a randomly chosen area of a Kanigen-coated beryllium mirror, shows surface roughness of this magnitude. The micrograph is made from a plastic replica of the surface, which has been shadowed with chromium at a nominal shadowing angle of 2.5°. Using this technique, it is difficult to resolve surface irregularities much smaller than 100 Å since the shadowing and replication technique itself introduces small-scale structures. Also, surface irregularities having slopes small compared to 2.5° cannot be detected. As can be seen from Figure 20, the surface is relatively free of local streaks and scratches.

The effect of these very small-scale irregularities could be to scatter incident X-rays through angles much larger than 10 min or, because of their steep slopes, to decrease the observed reflection efficiency by enhanced absorption. We believe, then, that the irregularities on the 100–200 Å scale of Figure 20 are not responsible for the fan-shaped patterns seen in Figure 19.

The angular resolution, considered the ability to separate closely spaced groups of point sources, is not as strongly dependent on local surface finish as one might expect. This is because the pattern produced in the focal plane by surface irregularities is a radial one, as demonstrated by Figure 19, in which contributions from the different elements about the circumference of the telescope all intersect at the nominal image position. Thus, the intensity distribution is strongly peaked at the center regardless of the quality of the local surface finish.

G. LIMITATIONS OF PRESENT SYSTEMS AND DIRECTIONS FOR FUTURE WORK

Existing mirror systems have exhibited X-ray resolutions of about 2 arc sec. The theoretical limits for such systems are the diffraction limit, which is on the order of 10^{-3} arc sec, and the limit imposed by geometric aberrations, which is less than 0.3 arc sec over a field of view 4 arc min in diameter. It is our belief that the difference between the theoretical and observed resolution can be attributed to the variation in the average slope around the circumference of the mirror and, to a lesser extent, to the deviation from the desired surface profile $S(x)$. In order to achieve the desired fractional arc second resolution in the future, it will be necessary to satisfy tolerances on the variation of average slope which are 5–10 times more stringent than those used to date. The tolerance on $S(x)$ will have to be a graded one, in which the allowed height of the deviation is proportional to the linear extent of the deviation as measured along the mirror surface. That is, it will be necessary to control slope deviations rather than height deviations. Also, the local surface roughness will have to be reduced to below 100 Å in order to achieve the maximum specular X-ray reflection efficiency. We believe that these specifications can be satisfied in the foreseeable future, and we are investigating methods of developing such systems.

We are studying the development of a large orbiting X-ray telescope having a fraction of an arc second resolution capability which would be used by many experi-

menters as a national facility. It appears feasible to develop a system with collecting area of about 1000 cm^2 by nesting many confocal telescopes one within another. The focal length would be about 6 m. Assuming reasonable improvements in surface finish through the use of other mirror materials and through advances in polishing techniques, we expect that about 20% of the incident flux can be focused in a 2 arc sec resolution element. The potential applications of such a system is discussed in Section 5.

3. Detection Techniques

In this section we will discuss some of the detection techniques which have been used or seem promising for use with focusing X-ray systems. The most important parameters of an imaging detector are spatial resolution, efficiency, dynamic range and storage capacity. The response of the device must be reproducible and capable of calibration; linearity is convenient but not absolutely necessary. The energy dependence of the response must be considered in selecting a system, but energy discrimination is usually achieved with other elements, such as filters or gratings rather than with the detector. It is somewhat academic and often misleading to compare the characteristics of various detection systems without considering the instrument being used and the experiment being performed. For instance, if one is trying to image a weak source such as a galactic X-ray source, the use of a high quantum efficiency and low intrinsic noise detector is almost mandatory. On the other hand, if one is trying to image the sun with a good size X-ray telescope and 1 arc sec resolution, one can adequately use film for the simultaneous storage of the 10^7 bits/sec reaching the focal plane. Furthermore, for space experiments, spacecraft considerations, such as jitter, available telemetry, particle and radiation environment, etc., become extremely important in the final selection of the optimum detector. For example, the high storage capacity of film will not be completely effective unless the vehicle jitter stability is smaller than the resolution element. With these limitations in mind, we will proceed to discuss some of the general characteristics of film and certain electronic imaging detectors.

A. FILM

Film, which is the oldest and most popular detector in conventional optics other than the eye, has also been extensively used with X-ray imaging optics. All but one of the X-ray telescopes flown to date have used film as the recording medium.

A commercial type of film consists of an emulsion layer supported by a base and coated with a few microns of gelatin for protection against mechanical abrasions. The gelatin topcoat will absorb soft X-rays and is the principle source of inefficiency at long wavelengths. The thickness of gelatin which will reduce the intensity of the incident radiation by $1/e$ is shown in Figure 21. This figure, which is based on absorption coefficients published by POUNDS (1965), indicates that the $1/e$ points for $\lambda = 6$ Å and 20 Å are 10 microns and 0.9 microns respectively. The silver halide of the emulsion is also embedded in gelatin (30–60%), which further reduces the sensitivity of the emulsion. The Ilford Special we have used in some of our flights had the following

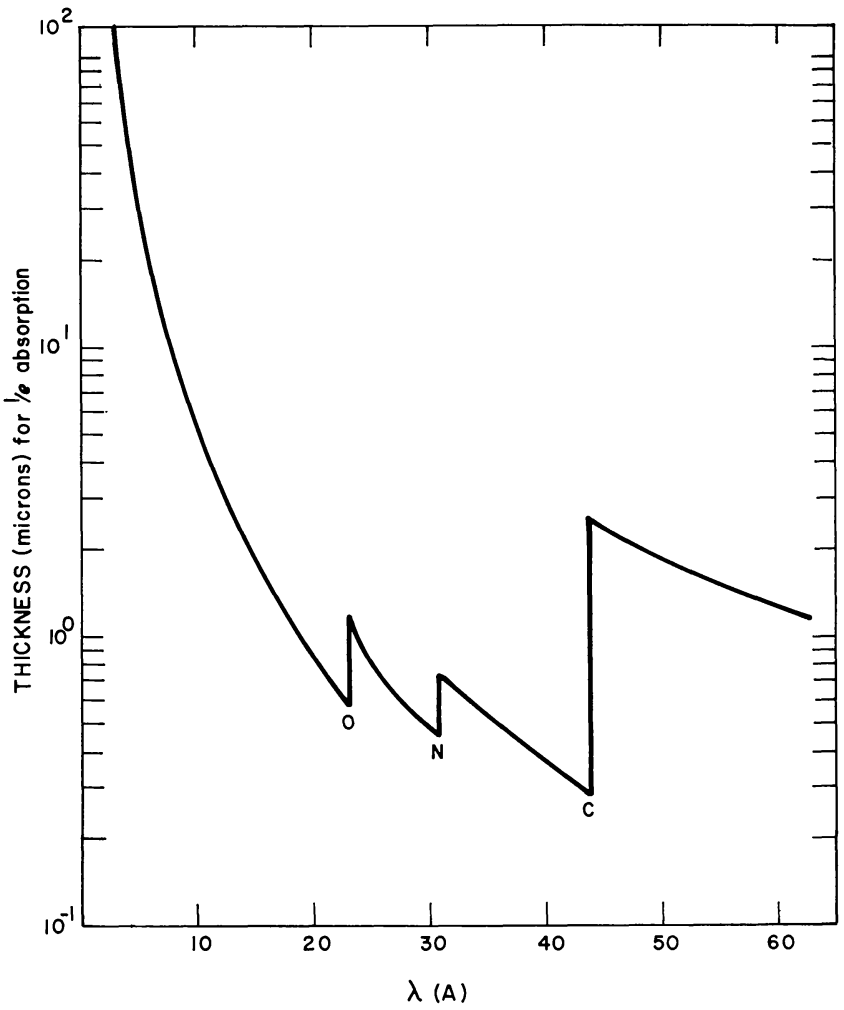

Fig. 21. Thickness of the gelatin topcoat on photographic film which will reduce the intensity of the incident radiation by a factor of $1/e$.

characteristics: gelatin supercoat 2 microns; emulsion thickness 12.5 microns (1.05 mg cm^{-2} gelatin and 1.50 mg cm^{-2} silver halides).

The trend of producing films for the detection of soft X-rays has been to eliminate the overcoat of gelatin and to increase the ratio of silver halide to gelatin in the emulsion. These films are delicate and may be damaged if conventional film transport systems are used. Careful camera design is required to avoid the problems of mechanical abrasion and electrostatic discharge when these films are used in roll form.

The response of soft X-radiation of several films has been extensively studied at several laboratories and in particular at Leicester University (POUNDS, 1965; ATKINSON and POUNDS, 1964) and AS&E (SZILAGYI and BLACKMAN, 1966; REIDY *et al.*, 1968). A great deal of additional unpublished work has recently been done in connection with the ATM manned mission by the Marshall Space Flight Center, the Goddard Space Flight Center and our laboratory. Figure 22 is a compendium of a series of 8.3 Å (Al Kα radiation) sensitivity measurements which were performed in

our laboratory (WIZA, 1968). The apparent toe to these curves at low flux levels is a consequence of the logarithmic plot and the difficulty of background subtraction at low flux levels. ATKINSON and POUNDS (1964) have shown that a single X-ray photon is adequate for sensitizing a grain; therefore, there is no minimum flux required for detection and also no reciprocity failure. The wide range of film sensitivities is quite evident; for example, the exposure required to obtain a net density of 0.5 varies from 2×10^7 to 10^9 photons cm^{-2} among the films for which data are presented. The density also will have a slight dependence upon the film batch, history and the develop-

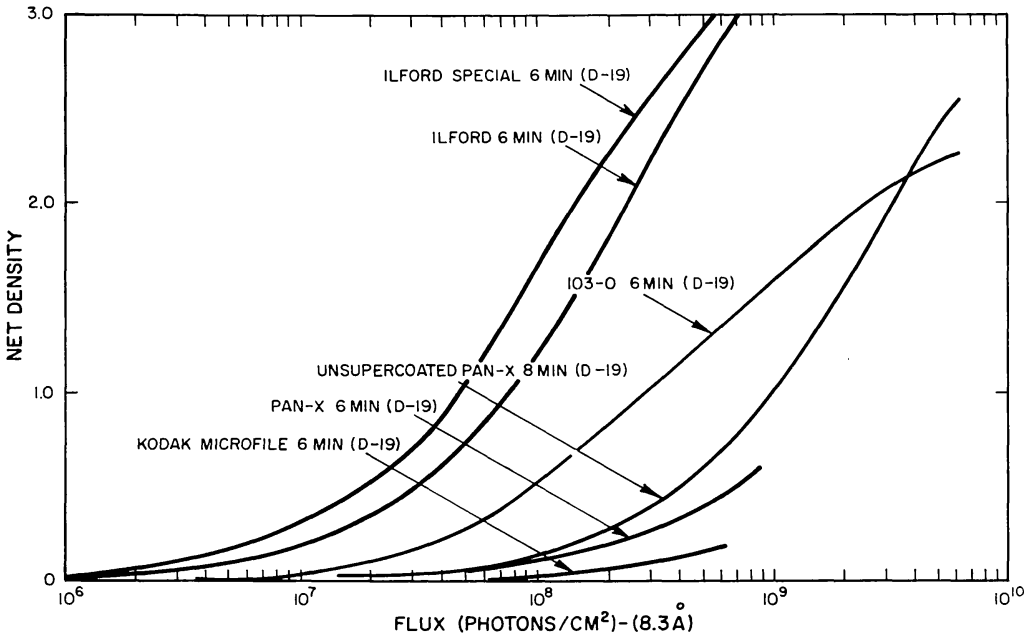

Fig. 22. The response of several photographic films to 8.3 Å radiation.

ment procedures. It is unfortunately not possible to calibrate the actual data film, and this remains a small source of error. Our practice is to make calibration test strips from the same batch as the data film; these test strips are pre-exposed to known X-ray flux levels and then developed with the data film.

The sensitivity curves are useful for planning an experiment so that optimum exposures are obtained, but the actual information limit of the film depends upon the spatial resolution, the number of photons required to develop a grain, the distribution of grains, and the background noise level or fog. Some characteristic film parameters are summarized in Table I. We have defined the resolution element as the smallest recognizable image. This depends only partially on grain size and, for fast film, depends primarily on how the grains cluster together.

Pounds has shown that the probability of an X-ray which is absorbed in the film emulsion resulting in a developable silver halide grain is between 0.5 and 1.0. However, the information yield is less than predicted by the above probability, because of the non-uniform grain distribution and other sources of film noise. The quantum

TABLE I

Parameters characterizing imaging detectors for X-rays

	Films		Image Dissector	Multi-channel array image. Intensifier/Film
	Fast	Slow		
Resolution element	20 microns	2 microns	40 microns (typical)	variable
Quantum efficiency	0.01		0.1	0.1
Dynamic range	10^3		10^5	10^5
Storage capacity	$> 10^8$ bits/cm^2		none	Depends on recording device
Noise	10 photons/res. el.		0.1 count/res. el. second	10^{-3} count/res. el. second
Linearity	No		Yes	Yes
Integrating capability	Yes Up to maximum density		$1/n$ of film or multichannel	Yes
Telemetry requirement	None		Moderate	Moderate[a]
Pointing requirement	jitter to be less than res. element for total exposure time		jitter to be less than res. element only for 1 raster	jitter to be less than res. element only for 1 raster period

[a] For the low stellar fluxes only moderate telemetry required to transmit the coordinates of each event.

efficiency of film in Table I is the 'effective quantum efficiency' which an individual photon detecting device would require to yield the same intensity error distribution as film of a specific exposure. An expression for the efficiency defined in this way:

$$\varepsilon = \frac{E}{A\,[\sigma_A(E)]^2} \approx \frac{1}{(EA)\,[\sigma_A(D)]^2}\left[E\,\frac{dD}{dE}\right]^2,$$

where ε is the efficiency. E is the number of X-ray photons/unit area, D is the density for exposure E, and $\sigma_A(D)$ is the rms variation in a density measurement made with sample area A and exposure E. The 'efficiency' value depends strongly upon the exposure because of the non-linear response of the film. The quantum efficiency thus defined is useful for comparing film with other systems as a detector for sources strong enough, so that the signal dominates the film background.

In the case of weak sources, the limit of sensitivity of the film is determined by the noise level. The noise consists of the initial background fog and the integrated background-radiation exposure prior to development. The initial fog level varies from film to film, but typically has a density of 0.1 or 0.2, which for the example of Ilford Special, is equivalent to an input of 10^6 photons/cm^2. If the film is carried in an orbiting satellite, one must consider the fogging resulting from the particle environment. Sensitivity studies of this kind have been conducted for the ATM flight at Marshall Space Flight Center (SKELTON and DELOACH, 1967). Table II from this study shows the number of days required to produce a background of 0.2 net density

TABLE II

Days to accumulate 0.2 net density in a 240 nautical mile at 30° inclination (SKELTON and DELOACH, 1967)

Shield thickness (gm/cm² Al)	2	5	10	20
Film	2	5	10	20
103-0	4.3	5.8	9.8	18
SWR (improved)	6.6	10	16	31
Plus-X	8.2	12	18	38
SC-5	11	15	23	42
SWR	21	41	60	130
Panatomic-X	34	49	87	170
SO-375	110	170	260	530

with shielding thickness of 2, 5, 10 and 20 mgs/cm^2 Al, for the ATM orbit (240 nautical miles, 30° inclination). The main contribution is due to the proton component during the passages through the South-Atlantic Anomaly.

The most important attractive characteristics of film are its spatial resolution, storage capacity, which is on the order of 10^8 bits/cm^2, simplicity, and long-period integration capacity. The photograph also makes large-scale structure and spatial relationships more apparent than any other method of presentation.

The most serious disadvantages of film are inadequate dynamic range, low effective quantum efficiency, high noise level, and lack of time resolution. The dynamic range is less than 10^3, and it is often impossible to perform meaningful measurements on two parts of the field simultaneously. The low effective quantum efficiency and high noise level reduce the sensitivity to weak sources. The lack of time resolution compounds the noise problem, as background elimination techniques such as anti-coincidence shields cannot be used; furthermore, the background is integrated for a period long compared to the data exposure. The film also must be recovered from the rocket or satellite but, as compensation, does not require telemetry during the experiment. It requires great effort to obtain quantitative intensity information from the film, and background subtraction is more difficult and less precise because of the non-linear response of the film.

B. ELECTRO-IMAGING SYSTEMS

In electro-imaging systems, the X-ray image is first converted to an electron image, which is then amplified and recorded electronically or converted to a visible light image and photographed. A variety of electro-imaging systems can be produced, but perhaps the basic distinction is between non-integrating and integrating devices. In a non-integrating device, a photon can be detected only when a particular resolution element is being scanned, whereas in an integrating device, the photon is recorded and stored between scans. The integrating device is thus more efficient by a factor equal to the number of resolution elements. We will discuss one non-integrating detector we have used and one integrating detector which we feel has a great potential in future applications.

1. *X-ray Image Dissector*

The image dissector, which is shown in Figure 23, is a non-integrating detector we have been developing for the ATM experiment. It will be used as a detector with a small X-ray telescope and provide a real time display of solar X-ray activity so that the astronauts can correctly point the primary telescope. The instrument is shown schematically in Figure 24. X-rays are focused onto a thin scintillation crystal which is coupled to the photocathode by a fiber optics face plate. The photoelectrons are electrostatically focused onto an aperture plate and only the electrons focused upon a small aperture hole are amplified and detected. The photocathode is scanned by

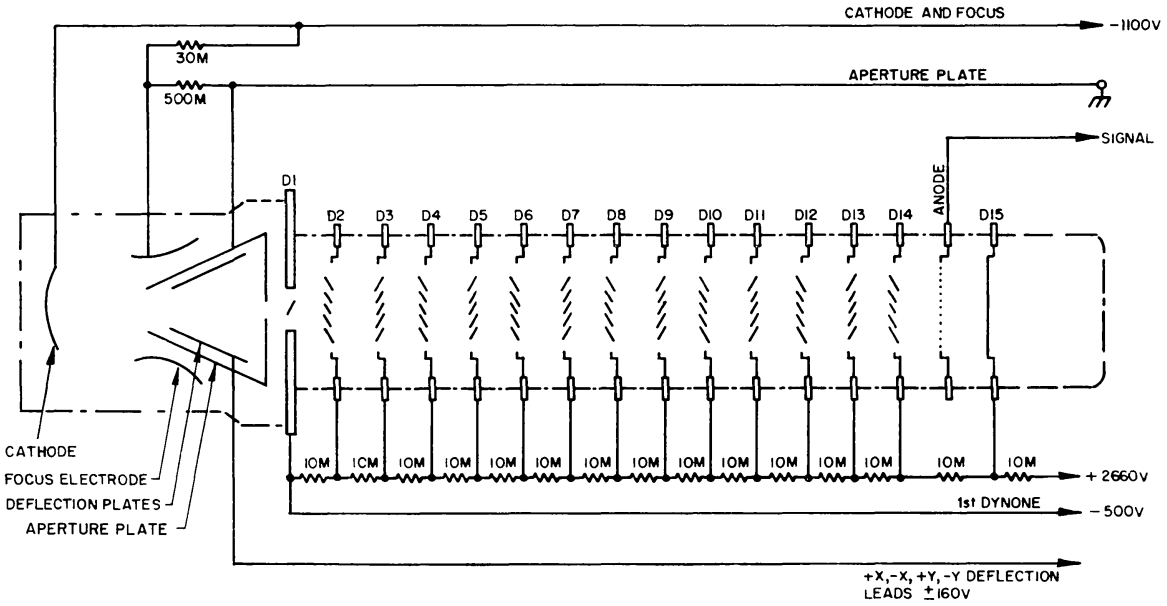

Fig. 23. Schematic diagram of the image intensifier. Photoelectrons from the cathode are electrostatically focused onto the flat surface of the aperture plate, forming an electron image of the cathode which is moved back and forth by the deflection fields. Electrons in that part of the image which overlays the hole in the aperture plate pass through into the electron multiplier section and are amplified. This is a non-integrating detector in which the signal from only one image element at a time is detected.

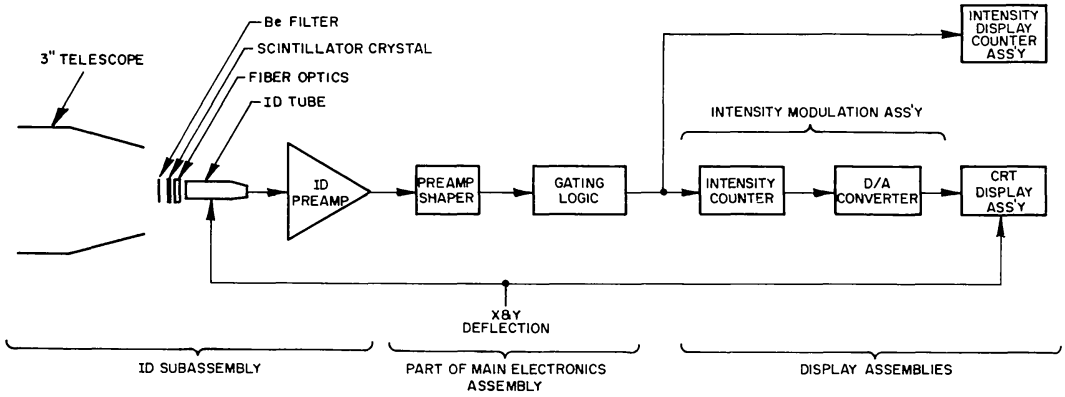

Fig. 24. Block diagram of the image dissector (ID) subsystems. The cathode ray tube (CRT) assembly will provide astronauts with a real-time display of solar flare activity during the Apollo Telescope Mount (ATM) experiment.

appropriately deflecting the electron image with the deflection plate fields, so that different sections of the photocathode can be imaged upon the aperture hole. At any given time, only one portion of the field is detected, and the information in other portions is lost. The principle drawback of the system is due to the loss of efficiency because of the short time of exposure per element. However, the system offers several advantages when one studies a strong source such as the sun and when only crude resolution is required so that the number of raster lines is small. These include low noise because only dark current from a small portion of the photocathode is detected, low telemetry requirements and simplicity.

In the ATM experiment, the electron-multiplier signal is used to modulate a cathode ray tube display; the deflection plates of the image dissector and cathode ray tube are driven synchronously, and thus an X-ray image of the sun is obtained. Approximately 1 sec is required for a complete image with about 1 arc min resolution (BALLAS *et al.*, 1968).

A variant of this system is presently being used in the OSO-4 X-ray spectroheliograph. In this system, the scanning is provided by spacecraft motion and the telescope field of view is defined by a small hole on the optical axis. The X-rays passing through the aperture impinge upon a Cs I photocathode; the resulting photo-

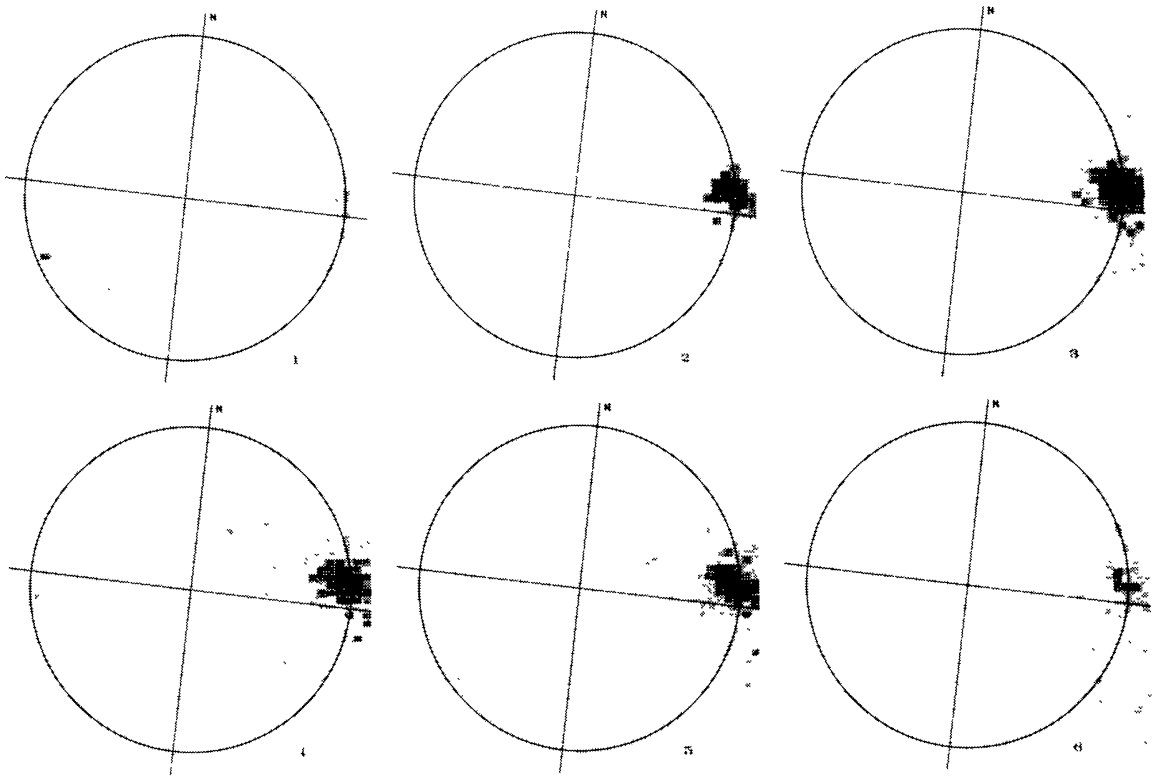

Fig. 25. A sequence of maps illustrating the growth and decay in X-rays of an importance 1 flare that occurred around 0825 UT, 28 October 1967. The times of the various stages of evolution of the flare are respectively for frames 1–6: 0645 UT, 0835 UT, 0855 UT, 0905 UT, 0915 UT, and 1015 UT. The peak observed intensity, sequence 2–3, was more than 20 times the pre-flare intensity. The diameter of the detector aperture is 1 arc min in this sequence obtained with the AS&E X-ray telescope on board the OSO-4 satellite. (PAOLINI *et al.*, 1968.)

electrons are electrostatically accelerated and detected by a NaI scintillator and photomultiplier. This system has obtained some 30000 images of the sun during the past 8 months (PAOLINI *et al.*, 1968). Figure 25 is a sequence of solar maps, illustrating typical data obtained by AS&E's X-ray telescope on OSO-4.

2. *Integrating Devices*

The signals in X-ray astronomy are small and the time available for observation is both limited and expensive; therefore, the use of integrating imaging detectors becomes almost mandatory. Several imaging tubes of this type, such as vidicons, orthicons, and secondary electron current tubes, which have been developed for visible light, can be adapted into X-ray imaging devices by the addition of a suitable X-ray converter. We refer to the excellent review of LIVINGSTON (1965) (specifically written for astronomical observations) for the characteristics of visible optics imaging devices. We are directing our present efforts in this area towards the development of an X-ray image intensifier system utilizing a microchannel plate as the detector.

The microchannel plate multiplier as described by GOODRICH and WILEY (1962), consists of an array of parallel small diameter glass tubes, as shown in Figure 26.

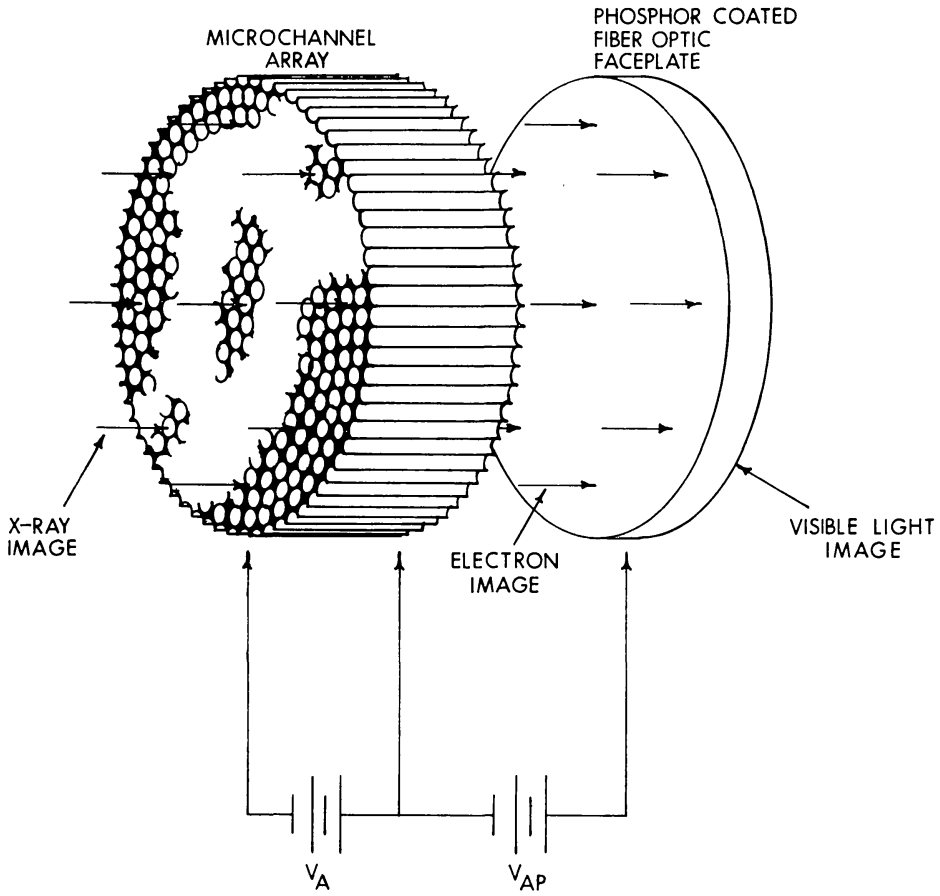

Fig. 26. X-ray image intensifier. The microchannel array consists of a bundle of small parallel tubes whose inner walls serve as photocathodes. A large gain results when the photoelectrons, accelerated axially down the tubes by an electric field, repeatedly strike the walls and generate secondary electrons.

The inner walls of the tubes are slightly conductive and have high efficiency for the emission of secondary electron. An electron in a tubelet is accelerated axially by an electric field; it will eventually strike the walls and generate additional secondary electrons, thus ultimately resulting in a large gain. The exit electrons may be detected directly or further accelerated into a phosphor screen to form a visible light signal, which can be photographed or detected with standard visible optics imaging devices. The electron gain is sufficient to detect single-photon events. The resolution is determined by the tube size, and by focusing properties of the exit electron detector. The loss due to focusing defects can be made negligible but is significant if the electrons are proximity focused onto the phosphor screen or other detector. The X-rays are detected by photoelectron production at the tubelet. The basic tubelet material has a quantum efficiency greater than 2% at 8.3 Å. It should be possible to increase the quantum efficiency to over 20% by coating the front of the array with a high-efficiency X-ray photocathode such as CsI, KCl or MgF (Lukirskii *et al.*, 1960).

This device has many potential advantages for space experiments. It is an imaging device with adequate resolution and high quantum efficiency. The cosmic-ray induced noise is also low because particles must traverse the small volume near the front of the device to be counted. The multiplier may be coupled to an integrating recorder such as film or a vidicon and thus achieve an imaging, single-photon detecting system with a dynamic range limited only by the recording device. The spacecraft-stability requirements are much less since the device is a single-photon detector and extended measurements can be made by superimposing short exposures properly translated to compensate for vehicle motion. The vehicle motion or jitter can also be removed by appropriately deflecting the exit electron image during the exposure.

Bendix, Rauland and Varian Associates in the U.S.A. and Mullard in England are presently developing these devices. We had the opportunity to test a prototype by Bendix with X-rays, and were able to detect individual photons without loss of resolution and verify the integration capability in a pulsed mode. No definite information is presently available on the ultimate values of the resolution, dark noise and quantum efficiency. The values we have listed in Table I are for the units which are presently being developed for our ATM experiments.

4. Spectrographic Techniques

Low-resolution spectral information can be obtained by non-dispersive techniques. The X-ray detector itself may be an energy-sensitive device such as a proportional or scintillation counter. Thin foils of various materials can be used as a set of broad band filters; this is the simplest possible device and has been used in many experiments with both focusing and non-focusing systems. Intermediate or high-resolution spectroscopy requires the use of dispersive elements. We will consider two techniques which are particularly suitable for use with grazing-incidence optics at soft X-ray wavelengths: X-ray slitless spectroscopy and crystal spectroscopy.

A. X-RAY SLITLESS SPECTROSCOPY

The slitless or objective grating spectrograph can be formed by placing a transmission grating in the ray path immediately ahead of or behind the X-ray telescope, as first proposed by GURSKY and ZEHNPFENNIG (1966). For each source in the field of view, this results in a real image (or zero-order spectrum) and, bracketing it, corresponding spectra of various orders. The system has moderate spectral resolution and is extremely efficient since all wavelengths and all sources in the field of view are examined simultaneously.

The spectral resolution, however, depends upon the size of the source feature; and in a complex field such as the sun, some information will be lost because of the overlays of different spectral orders from the several active regions.

The grating, which consists of an array of parallel absorbing strips, must either be free-standing or supported by a substrate thin enough to be transparent to the soft X-ray range of interest. The gratings we have developed have been supported by thin plastic substrates (ZEHNPFENNIG, 1966). The plastic layer is first formed on a thick replica of a conventional ruled grating by solvent casting (in the case of methylmethacrylate) or by precipitation from the vapor phase (in the case of parylene). The thin plastic layer is then stripped off and retains an impression of the grooves of the thick grating. The absorbing strips, which are the dispersing element of the grating, are formed on the plastic layer by a shadowing process in a vacuum evaporator, similar to the technique developed by BIRD and PARRISH (1960) for the fabrication of an infrared polarizer. This is illustrated in Figure 27. The substrate material used

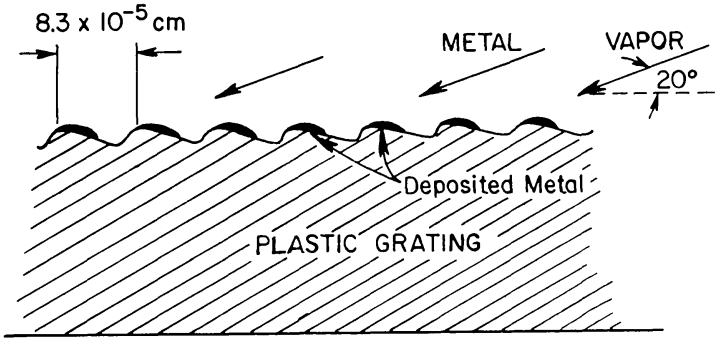

Fig. 27. Fabrication of a soft X-ray transmission grating. A thin plastic replica grating is shadowed at a low angle in a vacuum evaporator in order to produce a fine pattern of parallel absorbing strips.

in early gratings was methylmethacrylate. However, the thinnest layers which could be formed uniformly and removed intact from the thick grating were about 10 microns thick. Later work has emphasized the use of parylene, which has been used to fabricate gratings as thin as 5000 Å. In addition parylene has superior mechanical properties.

The limiting dispersion of transmission gratings intended for use in the 5–15 Å range is determined by the properties of the absorbing material. Because of the geo-

metry of the shadowing process shown in Figure 27, the thickness of the deposition obviously cannot exceed approximately one-half of the grating constant. Thus, the maximum thickness of the absorbing materials must decrease as the dispersion is increased. The limiting dispersion is reached when the strips become so thin that they cease to absorb more than a negligible fraction of the incident flux. The absorbing materials which permit the highest dispersion are those with the largest X-ray absorption per unit path length, such as gold, tungsten and platinum. We have fabricated 1440 line per mm gratings shadowed with gold with efficiencies as high as 9%; but the efficiency of similar 2880 line per mm gratings was found to be less than 1%. (The dispersions corresponding to 1440 lines per mm and 2880 lines per mm are 0.50 arc min per Å and 1.00 arc min per Å, respectively.) The term efficiency as used here is defined as the fraction of the incident power sent into one of the first-order spectra. The maximum theoretical efficiency is 20% for a grating with a completely transparent substrate and with completely absorbing strips of width one-half the grating constant. The low efficiency obtained with the 2880 line per mm grating is believed to be the result of the large inherent grain size in vapor-deposited gold

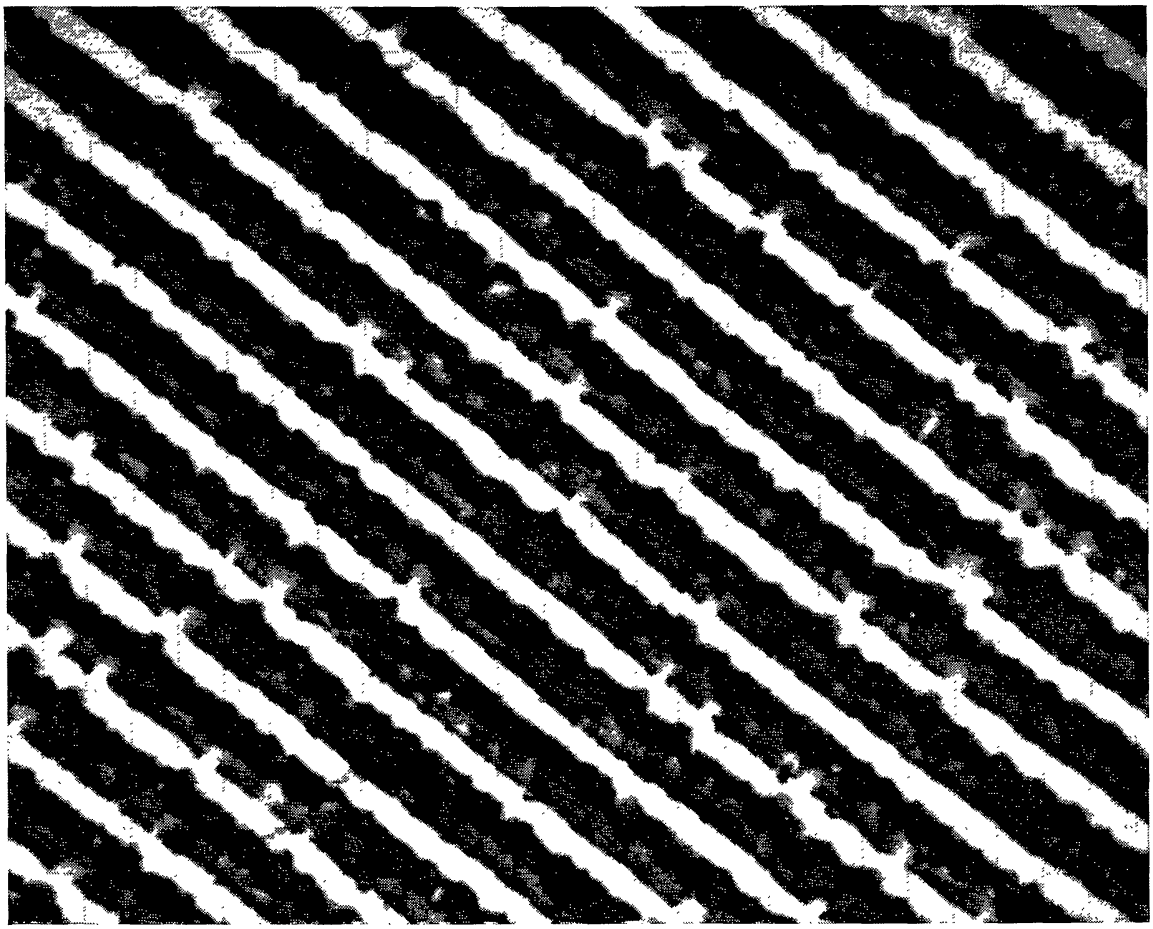

Fig. 28. Electron microscope picture of a small area of a gold-shadowed parylene transmission grating. The areas covered by the gold show up as dark strips on a light background. The center-to-center spacing of these strips is 7000 Å. Clumping and grain structure is evident within the strips.

films (BRADLEY, 1965) which causes the absorbing and transmitting areas of the grating to be poorly defined.

The effect of the grain size or clumping in the gold deposit can be seen on a 1440 line per mm grating in Figure 28. Another result of the large grain size is a decrease in the effective density of the gold layer. Platinum and tungsten deposits typically have finer grain structures and higher effective densities but are more difficult to evaporate in relatively thick layers (1000–2000 Å) on fragile substrates because of the high temperatures required. We expect, however, that the required evaporations can be performed with suitable equipment in the near future.

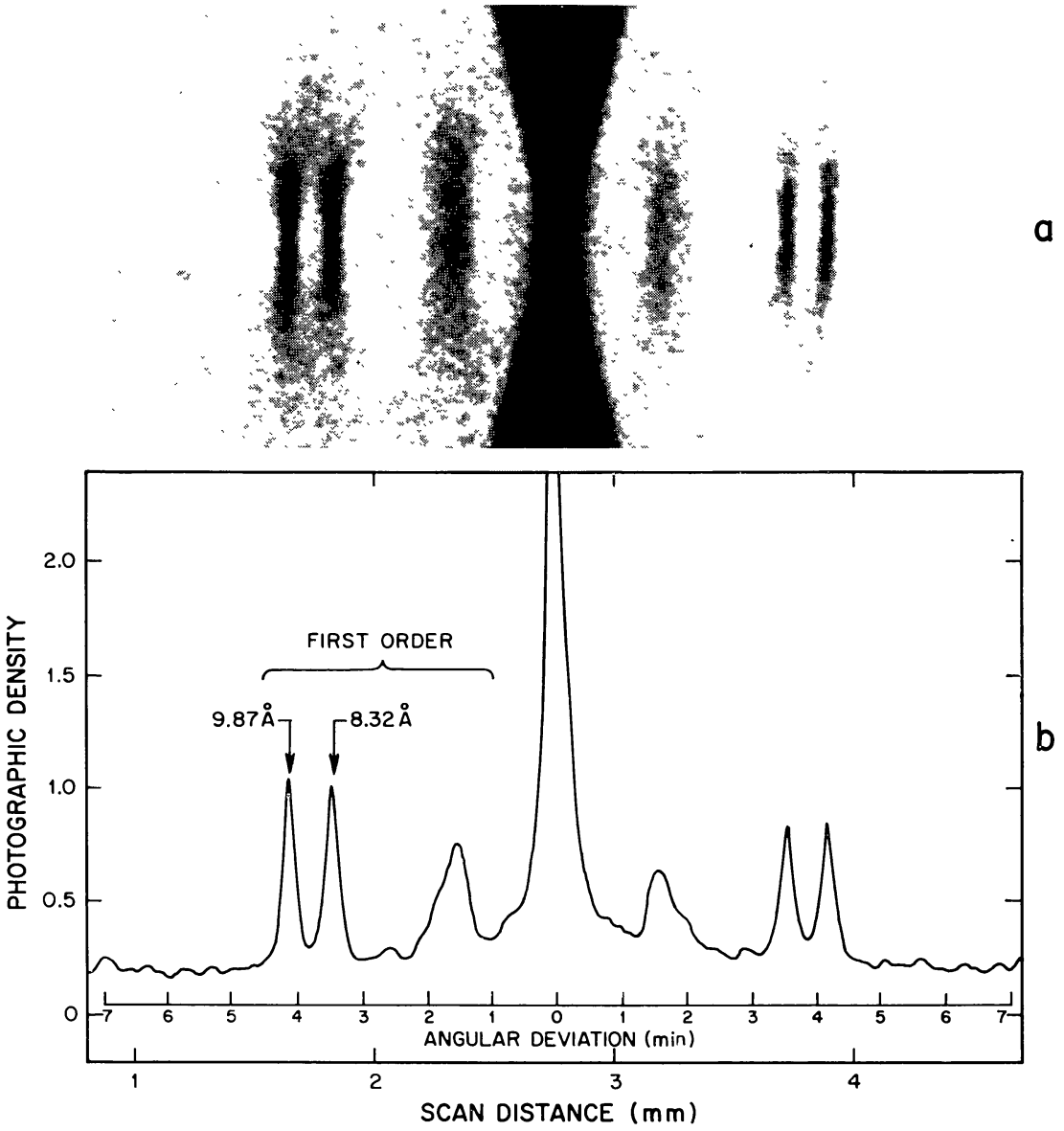

Fig. 29. An early slitless spectrograph exposure of a laboratory source which contained aluminum and magnesium. The aluminum and magnesium lines at 8.32 Å and 9.87 Å are easily resolved. The feature closest to the zero order is the continuum spectrum. Since the source voltage was 4.0 KV, the continuum has a short-wavelength cutoff at 3 Å.

Self-supporting gratings without substrates may be fabricated in the same manner as the Tübingen group Fresnel zone plates (MÖLLENSTEDT *et al.*, 1963). This technique is of great interest for longer-wavelength studies where the grating efficiency is limited by the X-ray transmission of the substrate.

Spectra of laboratory sources made with various versions of the slitless spectrograph are shown in Figures 29, 30 and 31. The spectral feature with the shortest wavelength recorded to date is the beginning of the continuum spectrum at 3.0 Å in Figures 29a and 29b. The long-wavelength response is shown in Figure 30, where

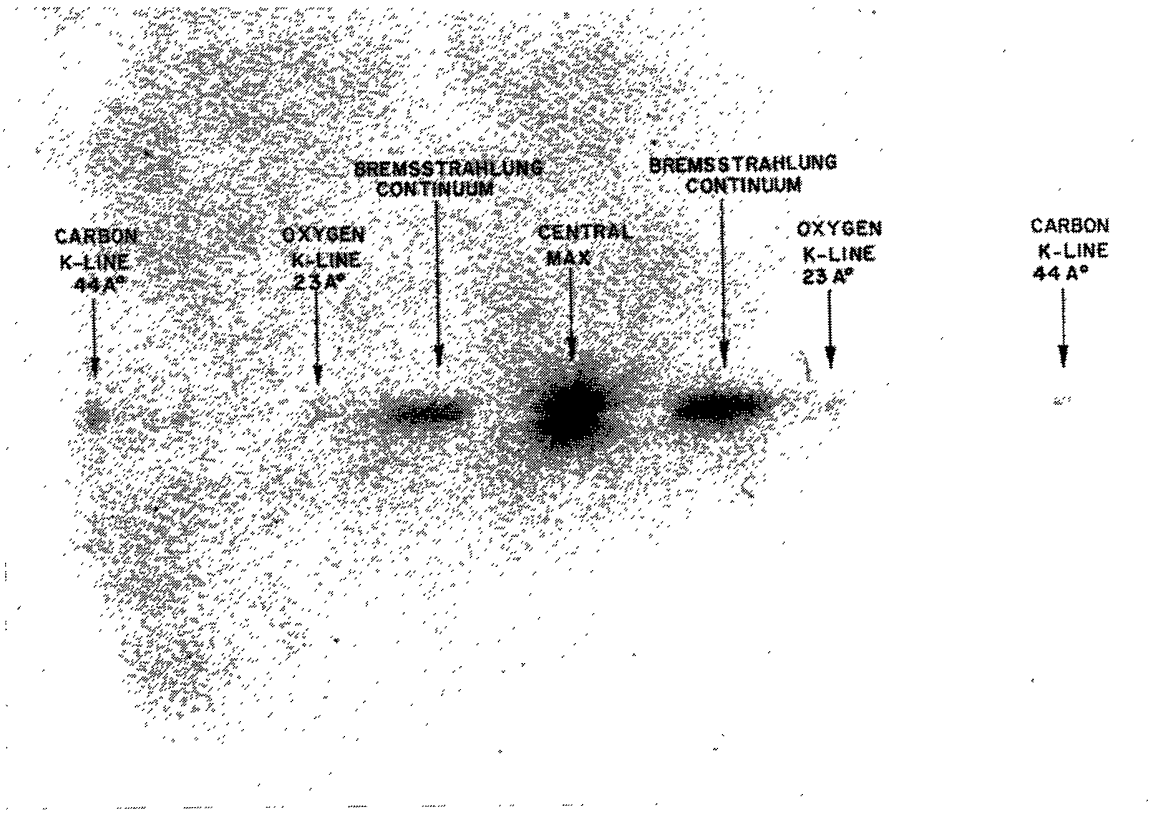

Fig. 30. A slitless spectrograph exposure illustrating the response at long wavelengths.

oxygen and carbon lines at 23 Å and 44 Å, respectively, can be seen. The spectral resolution of the instrument is illustrated in Figure 31, where the tungsten Mα and Mβ lines at 6.97 Å and 6.74 Å are clearly separated.

The first soft X-ray spectra of the sun produced by the slitless spectrograph were made 8 June 1968 on a sounding-rocket flight (VAIANA *et al.*, 1968). One of the exposures is reproduced in Figure 32. The grating was gold-shadowed parylene, 1 μ thick with 1440 lines per mm. There is little confusion among the many spectra of the flare and the plage regions; in general, the features are clearly separated. On the original negative, the most prominent line associated with the flare can be seen in the third-, fourth-, and fifth-order spectra at 9.2 Å. Fainter lines occur at 8.3 Å and 10.3 Å.

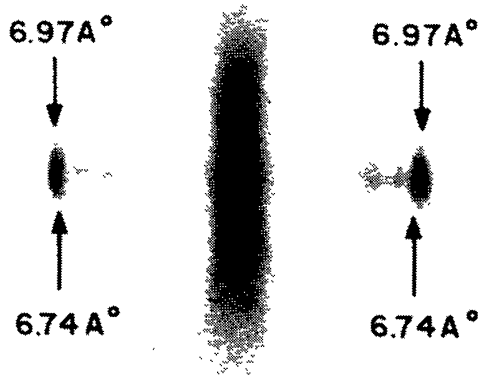

Fig. 31. Spectrum of a tungsten source showing the resolution of the tungsten Mα and Mβ lines at 6.97 Å and 6.74 Å, respectively. A resolving power $\lambda/\Delta\lambda$ of about 50 is indicated here.

B. CRYSTAL SPECTROSCOPY

Higher spectral resolution can be obtained using crystal spectroscopy. Non-focusing plane crystal spectrometers have been used extensively in solar studies (BLAKE *et al.*, 1965; NEUPERT *et al.*, 1966, 1967; EVANS and POUNDS, 1968; WALKER *et al.*, 1967).

However, there are two major disadvantages with such a system:

(1) For extended objects, there is confusion between the spatial and spectral distributions which significantly limits the obtainable spectral resolution.

(2) There is no focusing, and therefore the area of the detector and the corresponding noise level are large compared to those of a focusing system.

The problem of spatial and spectral overlay can be removed by the addition of a collimator before the crystal. Mechanical collimators with a field of view as small as 1 arc min have been built. However, it does not presently seem feasible to fabricate a mechanical collimator with a field of view considerably smaller than 30 arc sec. Higher resolution can be obtained by imaging the source using a grazing-incidence mirror, selecting the desired spatial element by placing a small aperture in the focal plane, and analyzing the transmitted radiation with a crystal and detection system. Such a system, which was suggested by SCHNOPPER and CLARK (1968), is shown in Figure 33. The aperture, crystal, and detector are mounted on the Rowland circle, which has a diameter equal to the radius of curvature of the crystal planes. This configuration has the property that, with a small spherical crystal, a monochromatic image of the aperture will be formed at the detector. The wavelength is determined by the Bragg condition and can be varied by appropriate motion of the crystal and detector about the Rowland circle. Since small detectors can be used with this system,

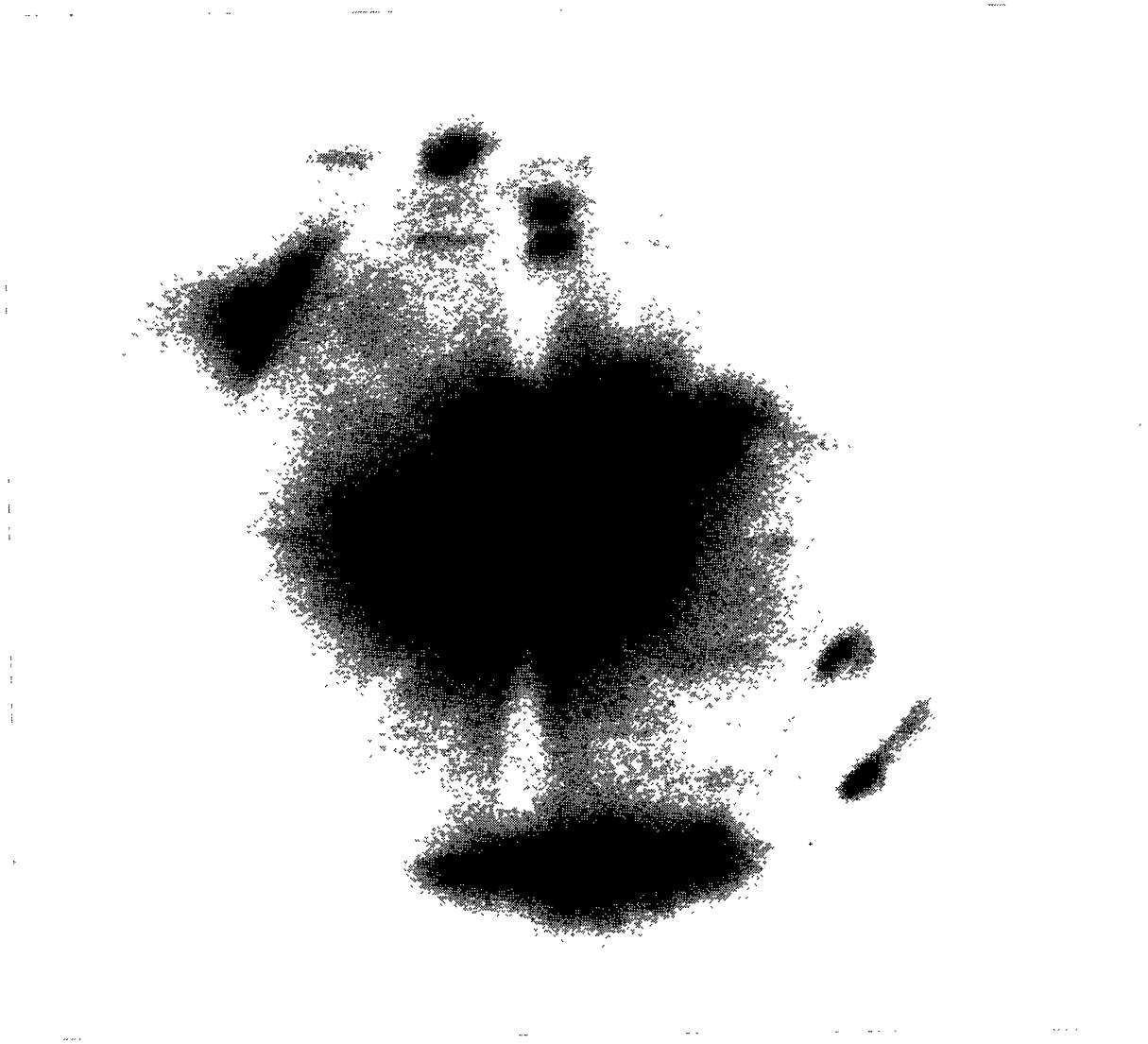

Fig. 32. Soft X-ray spectra of solar active regions produced by the slitless spectrograph on the flight of 8 June 1968. The exposure time was 60 sec. The grating was gold-shadowed parylene 1 micron thick, with 1440 lines per mm. The most prominent line associated with the flare was observed in the third-, fourth- and fifth-order spectra at 9.2 Å.

it will have a significant advantage in signal to noise ratio when compared to an equivalent-aperture non-focusing system. Schnopper and Clark have studied the aberrations associated with the Rowland-circle configuration and have shown that a spectral resolving power $(\lambda/\Delta\lambda)$ of 10^3 or higher can be obtained. The highest resolving power obtained to date with the slitless spectrograph is about 50.

The counting rate from an instrument of the type shown in Figure 33 is given by

$$CR = \int N(\lambda)\, A(\lambda)\, P(\theta, \lambda)\, \xi(\lambda)\, \mathrm{d}\lambda\,,$$

where $N(\lambda)$ is the incident flux from the selected spatial element, $A(\lambda)$ is the effective area of the telescope or the collecting area times the reflection efficiency, $\xi(\lambda)$ is the

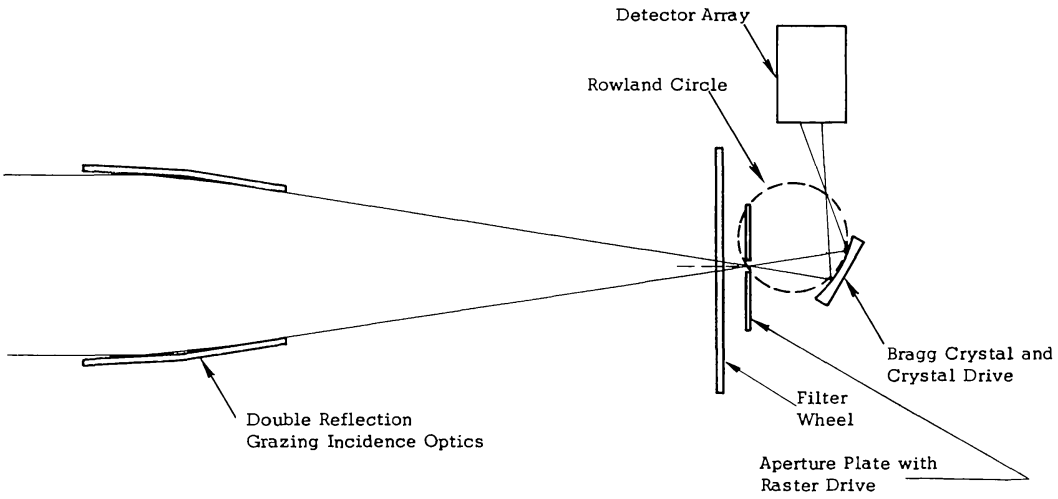

Fig. 33. Focusing spectrograph using an X-ray telescope and a spherically bent crystal.

detection efficiency, and $P(\theta, \lambda)$ is the reflection efficiency of the crystal for radiation of wavelength λ incident at a selected angle θ; $P(\theta, \lambda)$ is sharply peaked at the Bragg condition $2d \sin\theta = n\lambda$.

In measuring the line intensities in which the line width is narrower than the crystal-response function, the instrument would be centered on the Bragg angle θ_B and the counting rate would be

$$CR = N_{(\text{line})} A P(\theta_B, \lambda)\, \xi(\lambda).$$

If the line is wide compared to the crystal width, the line shape and total intensity can be determined by rocking the crystal over the angular region where the line radiation is efficiently reflected. If the angular scan is uniform, the average counting rate will be given by:

$$\overline{CR} \approx A(\lambda)\, \xi(\lambda)\, N_{(\text{line})}\, R(\lambda)/\Delta\theta, \tag{7}$$

where $R(\lambda) = \int P(\theta, \lambda)\, d\theta$ is the crystal reflection coefficient, $\Delta\theta$ is the angular scan width, and we have assumed that A, ξ, and R do not vary significantly over the line width.

TABLE III

Properties of crystals commonly used in soft X-ray diffraction experiments

	KAP	ADP	Calcite
2d	26.4 Å	10.64 Å	6.048 Å
Wavelength range	6–25 Å	2.26–10.1 Å	1.28–5.85 Å
Corresponding angular range	11.5–75°	11.5–75°	11.5–75°
F.W.H.M. of diffraction curve at indicated wavelength: 1.54 Å	–	–	5 arc sec
F.W.H.M. of diffraction curve at indicated wavelength: 4.94 Å	–	–	20 arc sec
F.W.H.M. of diffraction curve at indicated wavelength: 8.3 Å	–	40 arc sec	–
F.W.H.M. of diffraction curve at indicated wavelength: 10 Å	2 arc min	–	–
F.W.H.M. of diffraction curve at indicated wavelength: 20 Å	10 arc min	–	–
Reflection coefficient	2×10^{-5} radians	10^{-5} radians	10^{-5} radians

Representative properties of some crystals expected to be useful in X-ray astronomy are given in Table III.

It is obvious that the techniques of slitless spectroscopy and crystal spectroscopy are complementary. The first provides a rapid measure of the spectral shape with a medium resolution while the second is particularly suited for detailed studies of line profiles. In the following section we will consider the application of both these techniques to the problems of X-ray astronomy.

5. Application of X-Ray Telescopes to Stellar X-Ray Astronomy

We will consider some experiments which could be performed with two telescopes, Telescope A, which has a mirror identical to the existing ATM telescope mirror shown in Figure 16b, and Telescope B, which we are designing for a future stellar X-ray astronomy experiment program. The parameters of these telescopes, which are listed in Table IV, do not require any improvements in telescope construction except in efficiency, which is determined primarily by surface finish. We have assumed that 5% of the incident radiation will fall inside a 5 arc sec diameter circle in Telescope A, and 20% of the incident radiation will fall inside a 2 arc sec diameter circle in Telescope B. The increased performance represented by the specifications for Telescope B is reasonable for an instrument to be launched in the mid-seventies. The actual telescope resolution for strong sources will be better than 2 and 0.5 arc sec in Telescopes A and B, respectively. For the purpose of the calculations below, we have taken the resolution for Telescopes A and B to be 5 and 2 arc sec, respectively. Our estimates, therefore, represent a lower limit on the telescope performance.

TABLE IV

Telescope parameters

	Telescope A[a]	Telescope B[a]
Diameter (cm)	30.5	87
Focal length (meters)	2.1	6.1
Collecting area (cm^2)	44	1000
Field of view, diameter (degrees)	1	1
Point-source image distribution	5 % of incident flux imaged in 5 arc sec diameter circle	20 % of incident flux imaged in 2 arc sec diameter circle
Telescope resolution element (maximum size)	5 arc sec	2 arc sec
Net effective area in tel. resolution element (cm^2)[b]	0.22	20
Noise/telescope resolution element (counts/sec)	10^{-3}	10^{-3}
Number of telescope resolution elements in field	5×10^5	3×10^6
Wavelength resolution for 1440 lp/mm grating (Å)	0.17	0.067
Number of resolution elements in a dispersed spectra, 3–12 Å one side, one order	53	134

[a] The mirrors of Telescope A are identical to those which have been fabricated for the S-054 solar X-ray telescope experiment to be flown on the NASA Apollo Telescope Mount. Telescope B is a system we are designing for a stellar X-ray astronomy experimental program.

[b] Calculated on the basis of a detector efficiency of 10%.

A. DISCRETE POINT SOURCES

The sensitivity of the telescope to point sources is defined by the requirement that there be less than some specified probability that a background fluctuation could yield a given accumulation of events in an image element. There are 5×10^5 and 3×10^6 resolution elements in the fields of Telescopes A and B, respectively. If we require the probability be less than 1% that background fluctuation anywhere in the field simulate a source, then the required probability that a background fluctuation in a single resolution element simulate a source becomes 2×10^{-8} and 3×10^{-9} for Telescopes A and B. Consider two observational periods: a moderate observation lasting 10^3 sec or about 15 min; and a long observation lasting 5×10^4 sec or about 14 hours. The background per resolution element in available instrumentation is about 10^{-3} sec^{-1}, or averages 1 event and 50 events in the moderate and long exposures respectively. The number N of signal plus background events required to satisfy the source criteria for the 10^3 sec observation with Telescope A is obtained from $P(N \mid 1.0) = 2 \times 10^{-8}$, where $P(N \mid m)$ is the probability of obtaining N or more events when the mean number is m. The number of signal events required for each of our examples is listed in Row 3 of Table V. The equivalent minimum detectable flux is given in absolute units in Row 4 and as a fraction of the source Sco X-1* in Row 5. The distance at which a source like Sco X-1 could be detected is given in Row 6.

The value of the X-ray telescopes is immediately apparent upon an examination of this table. In a 1000 sec observation period with the ATM telescope, we could detect a source with only 4.5×10^{-4} the intensity of Sco X-1, or approximately 5 times fainter than any of the presently known sources, and also provide a location accurate to a few arc seconds. Any of the presently known sources could be detected in an observing time of 5 min, and an observational program to provide accurate

TABLE V

Telescope sensitivity for point sources

Telescope	A	A	B	B
(1) Observation time (sec)	10^3	5×10^4	10^3	5×10^4
(2) Number of expected background events	1	50	1	50
(3) Number of signal events required for 0.01 probability of a background fluctuation simulating the source anywhere in the field of view	10	44	11	47
(4) Min detectable intensity (photons cm^{-2} sec^{-1}) (1–4 keV)	4.5×10^{-2}	4×10^{-3}	5.5×10^{-4}	4.7×10^{-5}
(5) Min intensity [fraction of Sco X-1 (1–4 keV)]	4.5×10^{-4}	4×10^{-5}	5.5×10^{-6}	4.7×10^{-7}
(6) Distance at which a source like Sco X-1 could be seen (assuming 350 pc to Sco X-1) (pc) (not corrected for absorption)	1.6×10^4	5.5×10^4	1.5×10^5	5.1×10^5

* For the purpose of this calculation a flux of 100 photons cm^{-2} sec^{-1} between 1 and 4 keV is assumed.

locations for all of these sources would require little longer than the time required to point the telescope. Such a program would remove any doubts concerning present optical identifications. FRIEDMAN and BYRAM (1967) have claimed that the quasar 3C273 is an X-ray source with a flux of about 0.02 photons cm^{-2} sec^{-1}. A point source of this intensity known to be near 3C273 could be detected and accurately located in less than 1 hour, and this extremely important question would be resolved. Sources like Sco X-1 could be detected in any unobserved region of our galaxy with a 1-hour observation. This program would clarify the role of the X-ray sources in the evolution of galactic objects and provide many optical identifications which would allow investigation of these objects at other wavelengths. The statistical distribution of source intensities and the association of source intensities with other spectral characteristics can be better studied in galaxies other than our own where distance and local structure are so difficult to determine. A 14-hour observation with Telescope A would locate the Sco X-1 and Crab-like sources in the Magellanic Clouds. The same observational period with Telescope B would locate such sources in any of the local group of galaxies, perhaps a thousand sources would be found, and the association of the X-ray sources with the other galactic structural features could be determined. Finally, to come full circle, Telescope B would also enable us to study the coronal emission of more normal objects, including some near-by main sequence stars.

B. DIFFUSE SOURCES

The sensitivity of a telescope experiment to a diffuse source is determined by the requirement that the signal events be sufficient, so that the probability of a background fluctuation producing such an accumulation of events in the solid angle of the source is less than some probability P. This is an extremely conservative definition since the correlation between the X-ray distribution and the possibly known structure of the object has been ignored. If the background rate per unit solid angle is B, the source has a surface luminosity $d\phi/d\Omega$ spread uniformly over a solid angle Ω, the observing time is T, the effective area is A, and the solid angle corresponding to the field of view is Ω_0, then the expected numbers of signal and background events in Ω are $d\phi/d\Omega\, A\Omega T$ and $B\Omega T$, respectively. We have taken as a source criterion the requirement that the probability of a background fluctuation producing the expected source-event accumulation be less than $0.01/(\Omega_0/\Omega)$, where the solid angle factor approximately corrects for the number of positions in the field of view at which a background fluctuation could simulate a source. This criterion can be expressed as:

$$P\left[(B\Omega T + d\phi/d\Omega\, A\Omega T) \,\middle|\, B\Omega T\right] < 0.01/(\Omega_0/\Omega).$$

The minimum detectable total source intensity increases approximately as the square root of the source solid angle; therefore, the minimum detectable surface luminosity decreases approximately as the square root of the source solid angle. The dependence is not quite this simple because of the Poisson statistics and the factor of Ω in the right side of the above equation; some typical examples are given in Table VI.

TABLE VI

Telescope sensitivity for diffuse sources

Telescope		A	A	B	B
Observation time (sec)		10^3	5×10^4	10^3	5×10^4
	Source diameter (arc sec)				
Number of expected background events	5	1	50	6.25	312.5
	60	144	7200	900	45000
	240	2304	115200	14400	720000
Minimum no. of signal counts for a probability of 0.01 of background source simulation in a 1° diameter field of view	5	10	44	20	102.8
	60	59	390	141	969
	240	192	1338	475	3340
Minimum total intensity photons/cm² sec	5	4.5×10^{-2}	4.0×10^{-3}	1.0×10^{-3}	1.0×10^{-4}
	60	2.7×10^{-1}	3.5×10^{-2}	7.1×10^{-3}	9.7×10^{-4}
	240	8.7×10^{-1}	1.2×10^{-1}	2.4×10^{-2}	3.3×10^{-3}
Minimum detectable signal luminosity (photons/cm² sec arc sec²)	5	2.3×10^{-3}	2.0×10^{-4}	5.0×10^{-5}	5.2×10^{-6}
	60	9.5×10^{-5}	1.3×10^{-5}	2.5×10^{-6}	3.4×10^{-7}
	240	1.9×10^{-5}	2.7×10^{-6}	5.2×10^{-7}	7.4×10^{-8}

The Crab Nebula has a total flux of 16 photons cm^{-2} sec^{-1} in the 1–4 keV interval, or a surface luminosity of 1.4×10^{-3} photons cm^{-2} sec^{-1} arc sec^{-2} assuming a uniform emission over a 2 arc min diameter disk. This source would be quite visible in a 1000 sec observation. Since the surface luminosity is independent of distance, an object similar to the Crab could be observed at distances up to that which would result in a total intensity equal to the minimum detectable point source intensity. If we take the conservative estimate of 1100 pc distance to the Crab, sources like the Crab could be observed at a distance of 21 kpc with Telescope A in 1000 sec or up to 650 kpc with a 14-hour observation with Telescope B. Hence, such sources could reasonably be studied in our galaxy or the Magellanic Clouds with Telescope A and in the local group of galaxies with Telescope B. It may thus be possible to study the X-ray emission of supernova remnants in various stages of their evolution.

The structure of the Crab Nebula and similar objects could also be studied; for example, a point source in the Crab Nebula would satisfy the criteria that the probability of such a fluctuation anywhere in the Nebula is less than 0.01 in 14 hours with Telescope A, if it resulted in the emission in one telescope resolution element being increased by only 25%. Extended structural features, such as a long filament of higher emission, would be detected at flux enhancements appreciably less than the point source limit.

FRIEDMAN and BYRAM (1967) and BRADT *et al.* (1967) have reported an X-ray source within about 1° of the galaxy M-87. The surface luminosity corresponding to

the reported intensity evenly distributed over the 4 arc min diameter of M-87 would be about 4×10^{-6} photons cm^{-2} sec^{-1}, which would be detected in a few hours with Telescope A or in less than 1000 sec with Telescope B, and an accurate source position would be obtained which would allow an unambiguous identification of the X-ray source. It would also be possible to determine if the X-ray emission is reasonably uniformly distributed or is localized in smaller structures such as the 20 sec jet in that galaxy. In a 14-hour observation with Telescope B objects similar to M-87 but 35 times farther away would be observable. This should enable us to study such galaxies in various stages of evolution; perhaps we will obtain a better understanding of these galaxies and their possible contribution to the observed isotropic X-ray background.

1. *Low-Dispersion Spectroscopy*

In this section we will discuss some of the experiments which could be performed with a slitless spectrometer constructed of a transmission grating and a grazing incidence telescope. This system, as stated previously, is very efficient, since data in the entire spectral range of the instrument are recorded simultaneously for all sources in the field of view. The spectral resolution with gratings similar to those now constructed would be 0.17 Å and 0.067 Å for the telescopes being considered. This is sufficient for the detection of emission lines which would provide the crucial proof that the emission of a source is a thermal or quasi-thermal process rather than synchrotron radiation. The line intensities would yield information about temperature distributions and relative abundance of the elements in the emission region. It will also be possible to detect the long-wavelength cutoff and X-ray absorption edges which are proportional to the quantity of oxygen, neon and other elements present in the interstellar media.

Consider, for example, the detection of the NeX emission line at 1.02 keV in the spectrum of Sco X-1; this line is expected to be one of the stronger lines, and TUCKER (1967) has estimated its intensity to be 1.1 photons cm^{-2} sec^{-1} assuming the X-ray emission source to be bremsstrahlung in a hot thin plasma and neglecting interstellar absorption. The observed continuum at 1.02 keV is about 1.42 photons cm^{-2} sec^{-1} Å, and, in a 1000 sec observation with Telescope A, we would find an average total of 22 events per resolution element in the two first-order spectra assuming an ideal grating with a total of 40% of the incident power diffracted into the two first-order spectra. The minimum detectable number of events from an additional line source would be 20 to satisfy the criteria that the probability of such a fluctuation anywhere among the 53 resolution elements be less than 0.01. This corresponds to a minimum detectable initial flux of 0.091 photon cm^{-2} sec^{-1} compared to Tucker's theoretical value of 0.32 photons cm^{-2} sec^{-1} with the experimentally determined absorption factor of 0.29. Weaker lines or weaker sources would require longer observing times; the time for an observation scales as $(B + dN/d\lambda\, \Delta\lambda)/S_L^2$, where B is the background rate $dN/d\lambda\, \Delta\lambda$ is the continuum contribution in the telescope resolution element containing the line, and S_L is the line intensity. The minimum detectable intensities

in a 14-hour observation with Telescope A and B are 2.9×10^{-2} and 2.9×10^{-4} times the intensity of Sco X-1 with similar spectra and absorption, or 8.9×10^{-3} and 8.9×10^{-4} times the intensity which would be observed if Sco X-1 were in an unobscured region. If these models are correct, this spectral feature could be observed in all of the presently known sources with the smaller of our two telescopes. Other lines which should be detectable are Mg XII (1.47 keV), Si XIV (2.00 keV), and Si XVI (2.61 keV).

The detectability of an absorption edge in the spectra produced by interstellar or intergalactic gas is more difficult to evaluate. If $S(E)$ is the spectrum without absorption, the observed spectrum below and above an edge at E_0 will have the form:

$$N(E)\,dE = S(E)\exp\left[N_H\sigma_1(E_0/E)^{8/3}\right]dE \quad \text{for } E < E_0$$
$$N(E)\,dE = S(E)\exp\left[N_H\sigma_2(E_0/E)^{8/3}\right]dE \quad \text{for } E > E_0\,.$$

In the region of important absorption edges the source function $S(E)$ may be regarded as constant near the edge. It is then possible to determine the number N_H by comparing the intensities above and below an absorption edge.

We will evaluate the expected number of counts in the energy interval E_1 to E_0 and E_0 to E_2 determined by the criteria that the absorption at E_1 and E_2 is equal to the average of the high and low values at the edge, or approximately:

$$E_1 \approx E_0(\sigma_1/\bar{\sigma})^{3/8}$$
$$E_2 \approx E_0(\sigma_2/\bar{\sigma})^{3/8}$$
$$\bar{\sigma} = (\sigma_1 + \sigma_2)/2$$

The average counting rate on the two sides will differ by a factor of about

$$\exp\left[N_H\left(\frac{\sigma_1 - \sigma_2}{2}\right)\right] \equiv 1 - \delta\,.$$

For example, consider the neon absorption edge at 0.87 keV. In this case, $\sigma_1 = 280$, $\sigma_2 = 470$ barns per hydrogen atom cm^{-2}; the wavelength interval satisfying the above criteria is about 1.4 Å on either side of the edge. The three sigma criteria for detecting the edge becomes:

$$\bar{N} = 3\sqrt{2N + 2B}\,,$$

where $\bar{N}$ and B are the expected number of events in a 1.4 Å interval from the source and background respectively. For Sco X-1, at 0.87 keV $\bar{N}/AT \approx 0.94$ photon/cm^2 sec and the minimum detectable edge in a 14-hour observation with Telescope A corresponds to a $|\delta|$ of 0.072 or $N_H(\sigma_1 - \sigma_2) \approx 0.15$. Thus the minimum detectable absorption increment, using the graph of Bell and Kingston (1967), corresponds to about 8×10^{20} H atoms/cm^2 compared to a typical H density of 12×10^{20} atoms/cm^2 in this area. It is apparent that the smaller telescope is useful for absorption edge work with only the stronger sources. The source Cygnus X-2, for example, would require

approximately 60 times as long for an equivalent absorption edge sensitivity. On the other hand, the larger telescope with additional effective area factor of 91 could be used for such observations.

2. *High-Resolution Spectroscopy*

The highest X-ray spectral resolution is presently obtained with Bragg crystal spectrometers similar to the instrument discussed in Section 4. The resolution of the device is approximately $\Delta\lambda = \lambda \cot\theta \, \Delta\theta$, where $\Delta\theta$ is the width of the reflection curve. The quantity $(\Delta\lambda/\lambda)$ depends upon the crystal and the wavelength of the radiation, and is small for the smaller wavelengths being considered here; values of order 10^{-4} or better are typical for wavelengths less than about 8 Å. This corresponds to a Doppler motion of about 30 km sec^{-1}, and source phenomena associated with such velocities could be detected if spectral lines are present. Velocities of this magnitude or greater are observed in many binary star systems, and, if an X-ray source were a member of such a system, the X-ray line wavelength would show a periodic time dependence; it would thus be possible to identify which member of a binary system is the X-ray source, or to detect the presence of a dim companion which might have an appreciable effect on the structure of the X-ray source. The velocities associated with galactic rotation and high-velocity stars are also several times this observational limit and could be detected if the direction of motion is favorable. The surface rotation velocities of early stars are often over 100 km sec^{-1}; such a motion would result in an observable line broadening. The thermal broadening should also be detectable; for the silicon example below, the often quoted X-ray source temperature of 5×10^7 °C results in a thermal broadening (FWHM) of about 10^{-3}, or ten times the expected resolution. Microscopic turbulence would contribute to the line width and may be measurable.

The Si XVI 4.75 Å (2.61 keV) line is a typical emission which might be studied. In TUCKER's (1967) model the flux in this line is 0.5 photons cm^{-2} sec^{-1}. The average counting rate for such a source using Telescope B, a calcite crystal (Table III), and a rocking angle of 10^{-3} radians, which is consistent with the expected line width and crystal resolution, would be 0.1 sec^{-1} using Equation (7). The continuum flux measured from Sco X-1 is 8.58 photons cm^{-2} sec^{-1} Å^{-1}, which would contribute a background counting rate of about 6×10^{-3} counts sec^{-1} given by

$$B = A(\lambda)\,(\lambda)\,\mathrm{d}N/\mathrm{d}\lambda\,\mathrm{d}\lambda/\mathrm{d}\theta\,R(\lambda),$$

where the notation is the same as in Equation (7). The detector noise contribution can be minimized since the crystal spectrometer is a focusing device and small detectors can be used; an upper limit is 10^{-3} sec^{-1}, which results in a total background of about 7×10^{-3} sec^{-1}. Thus, in a 1000-sec observation, 100 line counts would be accumulated with a signal to noise ratio of about 14. This is sufficient to determine the general profile of such an emission line. The larger telescope example is therefore adequate for high-resolution spectroscopy of the stronger sources.

6. Conclusions

The use of grazing-incidence imaging optics for X-ray astronomy presents the opportunity for measurements of greater sensitivity and finer angular and spectral resolution than hereto achieved. The improvements are so substantial that they may provide a qualitative advance in our understanding of X-ray emission from solar and extrasolar sources. This type of imaging system will allow us to study the emission from celestial X-ray sources in the wavelength range from a few to 100 Å in the same detail as obtained in visible light by conventional astronomical techniques. These observations are important because of the number of interesting astronomical objects which emit copiously in the soft X-ray region.

Existing X-ray telescopes are capable of locating to within a few arc seconds X-ray sources as faint as 4×10^{-5} of Sco X-1 with a reasonable observation time and observing diffuse sources a thousand times weaker than the Crab Nebula. The list of experiments which can be performed include: the optical identification of all observable sources which have optical counter parts including sources suggested to be M-87, 3C273 and other peculiar objects; the observation of the structure of the Crab and that of similar extended objects within our own galaxy and in the Magellanic Clouds; the determination of the X-ray structure of M-87 (if identified); the detection of emission lines (if present) from all of the presently known sources; and the detection of absorption edges due to interstellar gas. Larger telescopes (1000 cm^2 collecting area) presently being designed will be able to extend many of these observations to sources in other members of the local group of galaxies and allow high-resolution spectroscopy of the stronger X-ray sources.

In our opinion this list documents the crucial role which grazing-incidence focusing optics will play in future of X-ray astronomy and emphasizes the need and the importance for the continued development and improvement of the instrumentation here reviewed.

Acknowledgments

We thank Bruno Rossi and Herbert Gursky for several stimulating discussions, Donald Yansen for recent data on the development of X-ray transmission gratings, and Joseph Wiza for film calibration data.

The experimental work reported for the first time in this paper has been performed under NASA Contracts NAS-59041, NASW-1555, and NASW-1700.

References

Atkinson, P. A. and Pounds, K. A.: 1964, *J. Phot. Sci.* **12,** 302.
Ballas, J., Knapp, G., Wiza, J., and Zehnpfennig, T.: 1968, *IEEE Trans. Nucl. Sci.* **NS-15,** 551.
Bell, K. L. and Kingston, A. E.: 1967, *Monthly Notices Roy. Astron. Soc.* **136,** 241.
Bird, G. R. and Parrish, M., Jr.: 1960, *J. Opt. Soc. Am.* **50,** 886.
Blake, R. L., Chubb, T. A., Friedman, H., and Unzicker, A. E.: 1965, *Astrophys. J.* **142,** 1.
Blanco, V., Kunkel, W., Hiltner, W. A., Lynga, G., Gradt, H., Clark, G., Naranan, S., Rappaport, S., and Spada, G.: 1968, *Astrophys. J.* **152,** 1015.

BOWYER, S., BYRAM, E. T., CHUBB, T. A., and FRIEDMAN, H.: 1964, *Science* **146,** 912.
BRADLEY, D. E.: 1965, in *Techniques for Electron Microscopy* (ed. by D. H. Kay), F. A. Davis Company, Philadelphia, p. 58.
BRADT, H., MAYER, W., NARANAN, S., RAPPAPORT, S., and SPADA, G.: 1967, *Astrophys. J. Letters* **150,** L199.
BRADT, H., NARANAN, S., RAPPAPORT, S., and SPADA, G.: 1968, *Astrophys. J.* **152,** 1005.
BYRAM, E. T., CHUBB, T. A., and FRIEDMAN, H.: 1966, *Science* **152,** 66.
COMPTON, A. H. and ALLISON, S. K.: 1963, in *X-rays in Theory and Experiment*, D. Van Nostrand Co., New York, Chapter IV.
EHRENBERG, W.: 1949, *J. Opt. Soc. Am.* **39,** 746.
ELLIOTT, S. B.: 1963, in *X-ray Optics and X-ray Microanalysis, Third International Symposium, Stanford, 1962* (ed. by H. H. Pattee, V. E. Cosslett, and A. Engström), Academic Press, New York, p. 215.
EVANS, K. and POUNDS, K. A.: 1968, *Astrophys. J.* **152,** 319.
FRIEDMAN, H.: 1967, *Ann. Rev. Nuc. Sci.* **17,** 317.
FRIEDMAN, H. and BYRAM, E. T.: 1967, *Science* **158,** 257.
GIACCONI, R. and ROSSI, B.: 1960, *J. Geophys. Res.* **65,** 773.
GIACCONI, R., GURSKY, H., and WATERS, J. R.: 1965, *Nature* **207,** 572.
GIACCONI, R., REIDY, W. P., ZEHNPFENNIG, T., LINDSAY, J. C., MUNEY, W. S.: 1965, *Astrophys. J.* **142,** 1274.
GIACCONI, R., GORENSTEIN, P., GURSKY, H., USHER, P. D., WATERS, J. R., SANDAGE, A., OSMER, P., and PEACH, J. V.: 1967a, *Astrophys. J. Letters* **148,** L129.
GIACCONI, R., GORENSTEIN, P., GURSKY, H., and WATERS, J. R.: 1967b, *Astrophys. J. Letters* **148,** L119.
GOODRICH, G. W. and WILEY, W. C.: 1962, *Rev. Sci. Instr.* **33,** 761.
GORENSTEIN, P., GIACCONI, R., and GURSKY, H.: 1967, *Astrophys. J. Letters* **150,** L85.
GOULD, R. J.: 1967, *Am. J. Phys.* **35,** 376.
GUENTERT, O. J.: 1965, *J. Appl. Phys.* **36,** 1361.
GURSKY, H. and ZEHNPFENNIG, T.: 1966, *Appl. Opt.* **5,** 875.
GURSKY, H., GIACCONI, R., GORENSTEIN, P., WATERS, J. R., ODA, M., BRADT, H., GARMIRE, G., and SREEKANTAN, B. V.: 1966, *Astrophys. J.* **146,** 310.
HAYAKAWA, S., MATSUOKA, M., and SUGIMOTO, D.: 1966, *Space Sci. Rev.* **5,** 109.
HENDRICK, R. W.: 1957, *J. Opt. Soc. Am.* **47,** 165.
HENKE, B. L.: 1960, in *X-Ray Microscopy and X-Ray Microanalysis, Second International Symposium* (ed. by A. Engström, V. E. Cosslett, and H. H. Pattee), Elsevier, Amsterdam.
KIRKPATRICK, P. and BAEZ, A. V.: 1948, *J. Opt. Soc. Am.* **38,** 766.
LINDSAY, J. C.: 1965, *Ann. Astrophys.* **28,** 586.
LIVINGSTON, W. C.: 1965, in *Advances in Electronics and Electron Physics, Third Symposium, London, 1965* (ed. by L. Marton), Academic Press, New York, p. 1967.
LUKIRSKII, A. P., RUMSH, M. A., and SMIRNOV, K. A.: 1960, *Opt. i Spektroskopiya* **9,** 262.
LUKIRSKII, A. P., SAVINOV, E. P., ERSHOV, O. A., and SHEPELEV, Yu. F.: 1964, *Opt. i Spektroskopiya* **16,** 310.
MANGUS, J. D. and UNDERWOOD, J. H.: 1968, *Appl. Opt.* (in press).
MCGEE, J. F.: 1957, in *X-Ray Microscopy and Microradiography* (ed. by V. E. Cosslett, A. Engström, and H. H. Pattee), Academic Press, New York, p. 164.
MÖLLENSTEDT, G., VON GROTE, K. H., and JÖNSSON, C.: 1963, in *X-Ray Optics and X-ray Microanalysis, Third International Symposium, Stanford, 1962* (ed. by H. H. Pattee, V. E. Cosslett and A. Engström), Academic Press, New York, p. 73.
MORRISON, P.: 1967, *Ann. Rev. Astron. Astrophys.* **5,** 325.
NEUPERT, W. M., MUNEY, W. S., and ADELMAN, S. J.: 1966, paper presented before the AAS, October, 1966.
NEUPERT, W. M., GATES, W., SWARTZ, M., and YOUNG, R.: 1967, *Astrophys. J. Letters* **149,** L79.
NIGAM, A. N.: 1965, *Phys. Rev.* **138,** A1189.
ODA, M., BRADT, H., GARMIRE, G., SPADA, G., SREEKANTAN, B. V., GURSKY, H., GIACCONI, R., GORENSTEIN, P., and WATERS, J. R.: 1967, *Astrophys. J. Letters* **148,** L5.
PAOLINI, F. R., GIACCONI, R., MANLEY, O., REIDY, W. P., VAIANA, G. S., and ZEHNPFENNIG, T.: 1968, presented at the Special Meeting of the AAS on Solar Astronomy, Tucson, February, 1968.

PARRATT, L. G.: 1954, *Phys. Rev.* **95,** 359.
PARRATT, L. G. and HEMPSTEAD, C. F.: 1954, *Phys. Rev.* **94,** 1593.
POUNDS, K. A.: 1965, *J. Phot. Sci.* **13,** 20.
POUNDS, K. A. and RUSSELL, P. C.: 1966, in *Space Res.* vol. VI, p. 34.
REIDY, W. P., VAIANA, G. S., ZEHNPFENNIG, T., and GIACCONI, R.: 1968, *Astrophys. J.* **151,** 333.
SANDAGE, A. R., OSMER, P., GIACCONI, R., GORENSTEIN, P., GURSKY, H., WATERS, J., BRADT, H., GARMIRE, G., SREEKANTAN, B., ODA, M., OSAWA, K., and JUGAKU, J.: 1966, *Astrophys. J.* **146,** 316.
SCHNOPPER, H. W. and CLARK, G. W.: 1968, presented at the 126th meeting of the AAS, Charlottesville, April, 1968, to be published in *Space Sci. Rev.*
SKELTON, R. D. and DELOACH, A. C.: 1967, Analysis of Radiation Damage to ATM Film, NASA TM X-53666, Marshall Space Flight Center, NASA, Huntsville, Ala.
STEWARD, G. C.: 1928, *The Symmetrical Optical System*, Cambridge University Press, London, p. 89.
STEWARDSON, E. A. and UNDERWOOD, J. H.: 1965, *Brit. J. Appl. Phys.* **16,** 1877.
ŠVESTKA, Z.: 1966, *Space Sci. Rev.* **5,** 388.
SZILAGYI, Z. and BLACKMAN, E.: 1966, *Phot. Sci. Eng.* **10,** 111.
TUCKER, W. H.: 1967, *Astrophys. J.* **148,** 745.
UNDERWOOD, J. H. and MUNEY, W. S.: 1967, *Solar Phys.* **1,** 129.
VAIANA, G. S., REIDY, W. P., ZEHNPFENNIG, T., VANSPEYBROECK, L., and GIACCONI, R.: 1968, *Science* **161,** 564.
WALKER, A. B. C., RUGGE, H. R., CHATER, W. T., and HOWEY, C. K.: 1967, *Trans. Am. Geophys. Union* **48,** 151.
WARREN, B. E. and CLARKE, J. S.: 1965, *J. Appl. Phys.* **36,** 324.
WOLTER, H.: 1952a, *Ann. Physik* **10,** 94.
WOLTER, H.: 1952b, *Ann. Physik* **10,** 286.
WIZA, J.: 1968, private communication.
YONEDA, Y.: 1963, *Phys. Rev.* **131,** 2010.
ZEHNPFENNIG, T.: 1966, *Appl. Opt.* **5,** 1855.